AFRL-RY-WP-TR-2017-0104

ELECTROMAGNETIC SCATTERING AND ANTENNA TECHNOLOGY (EMSAT)

Task Order 0003: Design of a Circularly Polarized, 20-60 GHZ Active Phased Array for Wide Angle Scanning

Carl R. Pfeiffer
Defense Engineering Corporation

Boris Tomasic
Multispectral Sensing and Detection Division
Antennas and Electromagnetics Technology Branch

AUGUST 2017
Final Report

AIR FORCE RESEARCH LABORATORY
SENSORS DIRECTORATE
WRIGHT-PATTERSON AIR FORCE BASE, OH 45433-7320
AIR FORCE MATERIEL COMMAND
UNITED STATES AIR FORCE

NOTICE AND SIGNATURE PAGE

Using Government drawings, specifications, or other data included in this document for any purpose other than Government procurement does not in any way obligate the U.S. Government. The fact that the Government formulated or supplied the drawings, specifications, or other data does not license the holder or any other person or corporation; or convey any rights or permission to manufacture, use, or sell any patented invention that may relate to them.

This report was cleared for public release by the USAF 88th Air Base Wing (88 ABW) Public Affairs Office (PAO) and is available to the general public, including foreign nationals. Copies may be obtained from the Defense Technical Information Center (DTIC) (http://www.dtic.mil).

AFRL-RY-WP-TR-2017-0104 HAS BEEN REVIEWED AND IS APPROVED FOR PUBLICATION IN ACCORDANCE WITH ASSIGNED DISTRIBUTION STATEMENT.

*//Signature//

JASON W. WILLIAMS, Program Manager
Antenna & Electromagnetic Technology Branch
Multispectral Sensing & Detection Division

//Signature//

NATHAN B. TERRY, Lt Col, USAF, Chief
Antenna & Electromagnetic Technology Branch
Multispectral Sensing & Detection Division

*//Signature//

TRACY W. JOHNSTON, Chief
Multispectral Sensing & Detection Division AFRL Division Name
Sensors Directorate

This report is published in the interest of scientific and technical information exchange, and its publication does not constitute the Government's approval or disapproval of its ideas or findings.

*Disseminated copies will show "//Signature//" stamped or typed above the signature blocks.

REPORT DOCUMENTATION PAGE

Form Approved
OMB No. 0704-0188

1. REPORT DATE *(DD-MM-YY)*	2. REPORT TYPE	3. DATES COVERED *(From - To)*
August 2017	Final	10 April 2015 – 10 April 2017

4. TITLE AND SUBTITLE
ELECTROMAGNETIC SCATTERING AND ANTENNA TECHNOLOGY (EMSAT)
Task Order 0003: Design of a Circularly Polarized, 20-60 GHZ Active Phased Array for Wide Angle Scanning

5a. CONTRACT NUMBER
FA8650-14-D-1714-0003

5b. GRANT NUMBER

5c. PROGRAM ELEMENT NUMBER
62204F/61102F

6. AUTHOR(S)
Carl R. Pfeiffer (Defense Engineering Corporation)
Boris Tomasic (AFRL/RYMH)

5d. PROJECT NUMBER
7622/3001

5e. TASK NUMBER
N/A

5f. WORK UNIT NUMBER
Y1AB

7. PERFORMING ORGANIZATION NAME(S) AND ADDRESS(ES)
Defense Engineering Corporation
4027 Colonel Glenn Hwy
Beavercreek, OH 45431

Air Force Research Laboratory, Sensors Directorate
Wright-Patterson Air Force Base, OH 45433-7320
Air Force Materiel Command, United States Air Force

8. PERFORMING ORGANIZATION REPORT NUMBER

9. SPONSORING/MONITORING AGENCY NAME(S) AND ADDRESS(ES)
Air Force Research Laboratory
Sensors Directorate
Wright-Patterson Air Force Base, OH 45433-7320
Air Force Materiel Command
United States Air Force

Air Force Office of Scientific Research Public Affairs
875 North Randolph Street, Suite 325, Room3112
Arlington, Va 22203

10. SPONSORING/MONITORING AGENCY ACRONYM(S)
AFRL/RYMH

11. SPONSORING/MONITORING AGENCY REPORT NUMBER(S)
AFRL-RY-WP-TR-2017-0104

12. DISTRIBUTION/AVAILABILITY STATEMENT
Approved for public release; distribution is unlimited.

13. SUPPLEMENTARY NOTES
The U.S. Government is joint author of the work and has the right to use, modify, reproduce, release, perform, display or disclose the work. PAO case number 88ABW-2017-2742, cleared March 31, 2017. Paper contains color.

14. ABSTRACT
The radiating aperture of a circularly polarized, active electronically scanned array (AESA) that operates from 20 GHz to 60 GHz and scans up to 60° from broadside is reported. Design guidelines for wideband arrays are briefly reviewed, and the linearly-polarized connected Vivaldi array is chosen as the radiating element due to its simplicity in design and fabrication. Infinite array simulations are used to characterize the performance of a linear-to-circular polarizer placed on top of a linearly polarized Vivaldi array. The transmission coefficient and axial ratio of the antenna-polarizer combination are roughly 60% and below 3 dB, respectively, across most of the band and for scan angles up to 60° from normal. The antenna efficiency and axial ratio degrade by 1 dB at some points near the edges of the band and/or at wide scan angles.

15. SUBJECT TERMS
ultra-widebannd (UWB), vivaldi array, linear-to-circular polarizer

16. SECURITY CLASSIFICATION OF:			17. LIMITATION OF ABSTRACT:	18. NUMBER OF PAGES	19a. NAME OF RESPONSIBLE PERSON (Monitor)
a. REPORT	b. ABSTRACT	c. THIS PAGE			Jason Williams
Unclassified	Unclassified	Unclassified	SAR	76	19b. TELEPHONE NUMBER *(Include Area Code)* N/A

Table of Contents

List of Figures

List of Tables

Table **Page**

1.0 Summary

The radiating aperture of a circularly polarized, active electronically scanned array (AESA) that operates from 20 GHz to 60 GHz and scans up to 60° from broadside is reported. Design guidelines for wideband arrays are briefly reviewed, and the linearly-polarized connected Vivaldi array is chosen as the radiating element due to its simplicity in design and fabrication. Two approaches for radiating circular polarization are considered. First, a dual-polarized array is fed with a 90° hybrid coupler. Next, a linear-to-circular polarizer is placed on top of a linearly polarized array. It is shown that the first approach, utilizing dual-polarized antenna arrays, has several technological hurdles that are difficult to address in a low-cost manner. Therefore, the second approach utilizing a linear-to-circular polarizer is explored in detail. Two different linear-to-circular polarizers are reported with unprecedented bandwidth and scan range. Infinite array simulations are used to characterize the performance of a linear-to-circular polarizer placed on top of a linearly polarized Vivaldi array. The transmission coefficient and axial ratio of the antenna-polarizer combination are roughly 60% and below 3 dB, respectively, across most of the band and for scan angles up to 60° from normal. The antenna efficiency and axial ratio degrade by 1 dB at some points near the edges of the band and/or at wide scan angles.

2.0 Introduction

There is a continual desire to develop electronically steerable antennas with wider bandwidths, higher operating frequencies, increased polarization diversity, higher radiated power levels, etc. The antenna architecture with highest performance is typically the active electronically scanned array (AESA), which is a phased array that integrates a transmitter-receiver module (TR module) at every radiating element. One attractive feature of an AESA is the modularity such that the radiating aperture can be designed independently of the TR module. Radiating apertures with high efficiency, decades of bandwidth, and dual polarizations have been developed previously [1, 2, 3]. However, these arrays typically operate below 20 GHz, where unit cells are on the order of centimeters in size. At these length scales, arbitrary geometries can be fabricated with high precision using low cost PCB processing techniques. However, there is also a strong desire to develop AESAs at mm-wave frequencies. Increasing the operating frequency enables higher communication data rates due to the increased absolute bandwidth. In addition, mm-wave radars can provide higher resolution images due to the reduced wavelength. However, reducing the operating wavelength from the centimeter to the millimeter regime introduces significant design challenges. In particular, the wavelength is only ~10-100 times larger than the minimum feature size that can be fabricated using standard printed-circuit-board (PCB) or low temperature co-fired ceramic (LTCC) processing techniques, which limits the design freedom. One method of addressing these fabrication challenges is to use clean room processing techniques which can achieve feature sizes on the order of 1 μm [4]. However, this approach is expensive and time consuming.

This report investigates the most promising options for realizing a broadband AESA at mm-wave frequencies. The goal here is to develop a radiating aperture that can operate from 20 GHz to 60 GHz and be easily integrated with TR modules. The array should radiate right-handed circular polarization, which ensures that its operation is independent upon its orientation. It is also desired that the array should operate at scan angles up to 60° from broadside to cover a wide field of view. An effort was made to ensure these specifications are useful for a wide range of applications, so that numerous arrays designs in the future can leverage insights provided by this report.

Although the TR modules have not been developed yet, it is possible to make some high level assumptions about their characteristics based on previous work. Operating at higher frequencies necessitates that the spacing between radiating elements should be scaled according to the wavelength. However, TR modules do not typically benefit from similar scaling laws. TR modules providing roughly 1 W/element are typically several millimeters in size and independent of the frequency. At mm-wave frequencies, it is difficult to fit a 2D array of TR modules on a single printed-circuit-board (PCB). Therefore, we immediately limit ourselves to array architectures consisting of vertically oriented PCBs, as shown in Figure 1. This topology allows each element to extend as far as needed in the z-direction (broadside direction) to satisfy space requirements on the TR modules and digital control lines. In addition, extending the PCBs in the z-direction makes it easier to realize wide bandwidth antennas. Since the array operates at relatively short wavelengths, it can be several wavelengths in thickness and still maintain a physically thin profile of several centimeters.

The array should also support high radiated power levels. It is estimated that the TR modules can generate 1 W/element. At cell sizes on the order of several millimeters, 1 W/element generates a high heat density that must be dissipated so that the TR modules are not damaged. The vertically oriented PCBs shown in Figure 1 are a natural geometry that allows cooling ducts to be placed between each PCB [5]. Thus, the radiating elements and RF feeds can be designed relatively independently of the cooling system. Note that several narrowband, low cost arrays have been reported at mm-wave frequencies by integrating a large number of TR modules into a single chip [6, 7]. However, these arrays can only radiate milliwatts of power. In contrast, the goal here is to radiate kilowatts of power.

Two different radiating apertures are considered in this report. First, a dual-polarized antenna array is fed with a 90° hybrid coupler to generate circular polarization, as shown in Figure 1(a). This approach is more conventional at lower frequencies. However, it is shown here that there are several problems with scaling this design to mm-wave frequencies. In particular, it is difficult to physically implement this geometry due to restricted space per radiating element. In addition, these types of arrays typically have poor performance (axial ratio and matching) at large scan angles. Therefore, a second approach is considered that combines a linearly-polarized antenna array and a linear-to-circular polarization converter, as shown in Figure 1(b). The main challenge associated with this second approach is that a broadband linear-to-circular polarizer that operates at wide scan angles has not been realized before. Here, we show through simulation and experimentation that it is possible to realize a linear-to-circular polarizer with decent performance. Therefore, the second approach seems to be the most appropriate.

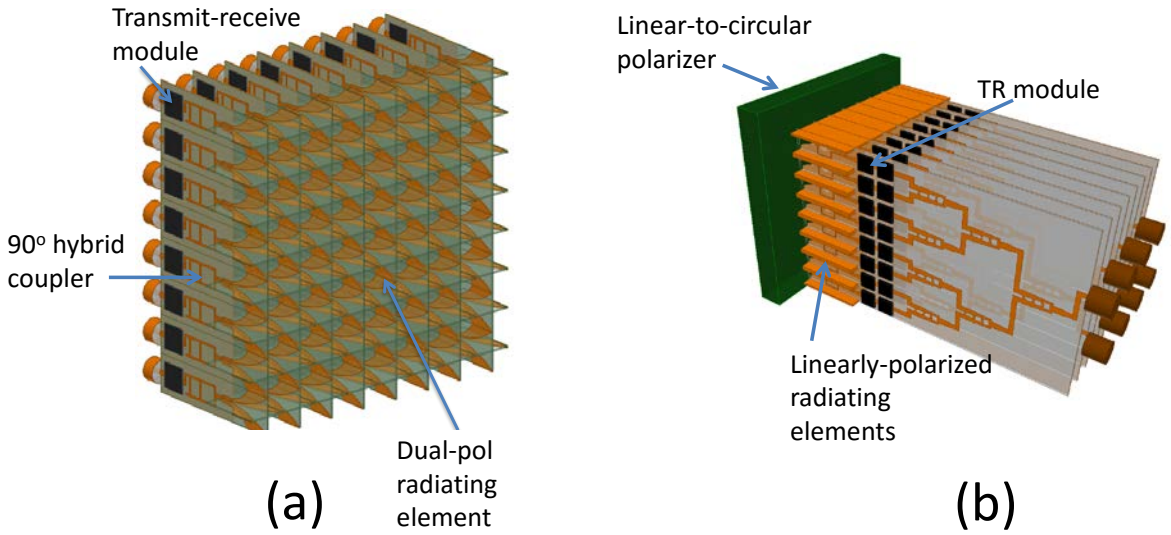

Figure 1: Generic Phased Arrays Where Each Radiating Element is Fed by a PCB Column

This reports is divided into several sections. In Section 3.0, wideband linearly-polarized antennas are reviewed. These antennas are strongly coupled, or connected, to their neighbors to approximate a current sheet with extremely wide bandwidth. Vivaldi arrays and connected dipole

arrays are considered. Both arrays can satisfy the bandwidth requirements outlined. The Vivaldi array is recommended for mm-wave applications since it simpler to design and more immune to fabrication imperfections. Some of the common drawbacks of Vivaldi arrays are their long electrical length and poor cross polarization. In our application, the electrical length is not too much of a concern due to the small wavelength. The high radiated cross-polarization is addressed by utilizing short Vivaldi elements that radiate in a quasi-parallel plate environment. In addition, dielectric matching layers are used, which improves polarization purity.

In Section 4.0, the approach shown in Figure 1(a) is considered, where an array of 90° hybrid couplers feeds dual-linear polarized antennas. This section focuses on the issues associated with the dual-linear polarized aperture. First, it is noted that the phase centers of the vertical and horizontal polarizations are not co-located in the conventional egg-crate array. Therefore, the egg-crate array cannot be fed with a 90° hybrid to radiate circular polarization at different scan angles. Next, dual-polarized antennas with co-located phase centers are analyzed. It is shown that these arrays support even modes that must be dissipated or undesired resonances will form when the array is scanned. Several methods of dissipating these even modes are mentioned, but they would be difficult to implement at mm-wave frequencies using PCB processing techniques. It is also emphasized that fabricating a dual-polarized antenna is inherently challenging if we require that it is fed with a planar PCB column as shown in Figure 1.

The issues associated with designing a dual-linear polarized array at mm-wave frequencies led us to consider the approach shown in Figure 1(b). In this approach, a linearly-polarized antenna illuminates a linear-to-circular polarizer to radiate circular polarization. Section 5.0 discusses the design of linear-to-circular polarizers with multiple octaves of bandwidth, which have not been reported to date. First, a polarizer utilizing cascaded anisotropic metamaterials is designed. However, this polarizer is quite bulky. Therefore, a second polarizer is designed using cascaded sheet impedances. This polarizer is approximately 1/3 the thickness of the cascaded metamaterial polarizer, and achieves a similar performance. Both polarizers work at incident angles up to 60° from normal.

Section 6.0 reports on the performance of the radiating aperture when the linearly-polarized Vivaldi array is combined with the linear-to-circular polarizer. Infinite array simulations are reported here, but design guidelines for realizing finite arrays are also discussed. It is shown in simulation that in the limit the array is infinitely large, the expected antenna efficiency and axial ratio are greater than 60% and below 3 dB, respectively. The antenna efficiency and axial ratio degrade by 1 dB at some points near the edges of the band and/or at scan angles near 60° from broadside. A 1:256 beamforming network is designed to feed each element. A concrete picture of the entire system is shown in Figure 51. Finally, some concluding remarks are made and future work is outlined.

3.0 Wideband, Linearly Polarized Arrays: Vivaldi and Connected Dipoles

3.1 Introduction

This section reviews initial simulations that were performed to investigate wideband radiating elements for the array. Several illustrative examples are discussed to provide intuition regarding the various antenna approaches. The advantages and disadvantages of each design are highlighted. None of the antennas are optimized, but the reported tradeoffs are useful for choosing an appropriate topology.

Wideband antenna arrays can be viewed as an impedance matching network from 50 Ω transmission lines to free space radiation with wave impedance of 377 Ω at broadside. This broadband match is generally accomplished by gradually tapering the impedance in several sections. Mutual coupling between array elements is often considered undesirable for narrowband arrays. However, the situation is different when multi-octave bandwidth and wide scanning capabilities are desired. In this case, it is almost imperative to use strongly coupled (or even connected) elements, which can approximate a current sheet [8] [9]. In this section, the definition of cross polarization and Marchand baluns are first reviewed. Then, connected Vivaldi arrays and tightly coupled dipoles are investigated. Their performance at broadside and scanning to 60° in the E, H, and diagonal (D) planes is reported. It should be noted that although it is desired to have an array that performs well at 60° scan, we do expect to see some degradation in performance at these extreme angles. Only infinite arrays are considered here, which require orders of magnitude fewer computational resources than finite arrays. In practice, finite arrays can realize similar performance as infinite arrays, provided several dummy cells are placed along the periphery. All reported simulations were performed with ANSYS HFSS. A waveport excites the microstrip line on the antenna, and the radiation is received by a Floquet port. It should be noted that the antennas in this section are y-polarized, whereas in later sections they are rotated to be x-polarized.

3.2 Definition of Cross Polarization

The radiated polarization purity is important for our application. However, all phased arrays radiate some cross polarization, especially when scanning in the diagonal planes. There are different methods of defining co- and cross-polarization. Throughout this report we will use the 3rd definition of cross-polarization as outlined by Ludwig [10], which is the most commonly used definition. The co- and cross-polarizations in Ludwig's 3rd definition are,

$$\begin{aligned} \boldsymbol{i}_{co} &= \sin(\phi)\,\boldsymbol{\theta} + \cos(\phi)\boldsymbol{\phi} \\ \boldsymbol{i}_{cr} &= \cos(\phi)\,\boldsymbol{\theta} - \sin(\phi)\boldsymbol{\phi} \end{aligned} \tag{1}$$

where $\boldsymbol{i}_{co},\ \boldsymbol{i}_{cr},\ \boldsymbol{\theta}$ and $\boldsymbol{\phi}$ are unit vectors. A unit cell simulation using HFSS terminated with Floquet ports provides the field that is transmitted in the TE and TM polarizations rather than co-

and cross-polarizations. Here, the radiating aperture is normal to the z-direction, in which case TE and TM polarizations are defined such that $\boldsymbol{i}_{TE} = \boldsymbol{\phi}$ and $\boldsymbol{i}_{TM} = \boldsymbol{\theta}$. Therefore, the co- and cross-polarizations can be expressed as,

$$\begin{aligned} \boldsymbol{i}_{co} &= \sin(\phi)\,\boldsymbol{i}_{TM} + \cos(\phi)\boldsymbol{i}_{TE} \\ \boldsymbol{i}_{cr} &= \cos(\phi)\,\boldsymbol{i}_{TM} - \sin(\phi)\boldsymbol{i}_{TE} \end{aligned} \tag{2}$$

3.3 Marchand Balun

The most common microwave transmission lines are unbalanced (e.g., coax, microstrip, stipline), meaning the current distribution on the signal trace and ground plane are different. However, antennas typically require a balanced feed for high polarization purity and broadband impedance match. Therefore, a balun must be designed that converts the unbalanced feed into a balanced source [11]. Wideband antennas most commonly utilize Marchand baluns which provide multiple octaves of bandwidth within a relatively compact geometry. An example of a Marchand balun is shown in Figure 2(a), where a microstrip transmission line at the left is converted into balanced strips at the right. The balun utilizes a slit in the ground plane to symmetrically feed the balanced transmission line at the right. The circular patch in the top conductor of the microstrip line and the circular opening in the ground plane are roughly $\lambda/4$ in size. The bandwidth is generally increased as the capacitive coupling between the circular end of the microstrip line and the ground plane (i.e., balanced strips) is increased. The reflection and transmission coefficients of the balun are shown in Figure 2(b). Even though the geometry is not optimized, the balun provides a broadband match. These baluns can easily realize the 3:1 bandwidth that we desire for our application, and will be used to feed all antennas in this report.

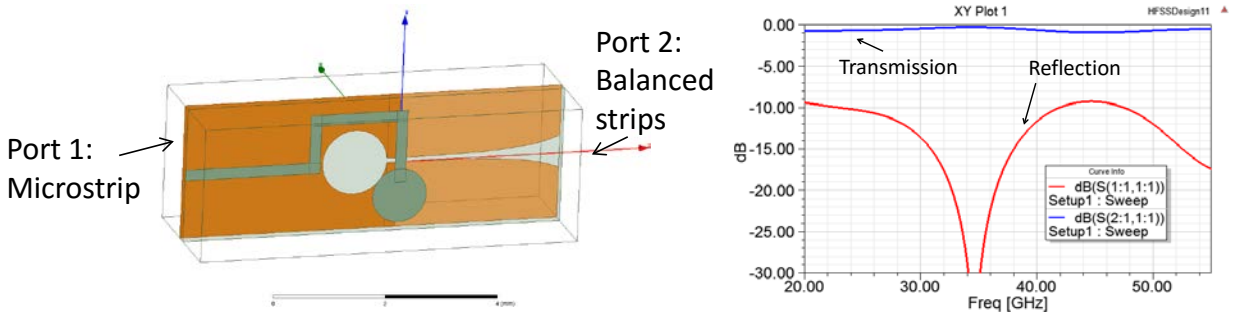

Figure 2: Unoptimized Marchand Balun Geometry (a) and Performance (b)

3.4 Vivaldi Array

Perhaps the most common wideband antenna array is the Vivaldi array, as shown in Figure 3(a). Vivaldi arrays are easy to design since their exponential taper is a natural geometry for providing a broadband impedance match between the transmission line feed and free space. In addition, their performance is relatively robust to fabrication imperfections. The periodicity in the

transverse plane determines the upper operating frequency, while the length of the element determines the lower operating frequency. Bandwidths on the order of a couple octaves can be realized if the length of the Vivaldi element is ~$\lambda_h/2$, where λ_h is the wavelength at the highest operating frequency [3]. Vivaldi arrays with a decade of bandwidth are not uncommon [1].

The periodicity in the transverse plane (xy plane) of the Vivaldi arrays reported in the following examples is 2 mm x 2 mm, which suggests that the array should be able to operate up to 75 GHz without exciting surface waves under ideal conditions. An ideal design maximizes the spacing between radiating elements to reduce TR module cost/area. A well designed connected array should have an element spacing that is only slightly lower than $\lambda_h/2$. In the following examples, the length of the exponential taper is 2 mm ($\lambda_h/2.5$). Each unit cell is fed with a 50 Ω microstrip line at port 1, which excites the Marchand balun. The balanced strips at the output of the balun are then exponentially tapered to realize a broadband impedance match to free space. Next, several Vivaldi designs are reported to provide some intuition into their design and performance.

3.4.1 Design 1: Basic Connected Vivaldi Array

A unit cell of the first design is shown in Figure 3(a). This design is sometimes referred to as a connected array since each unit cell is connected in the y-direction to the adjacent cells. Therefore, we expect strong mutual coupling between elements in the E-plane (yz-plane). Copper sheets normal to the y-direction are placed at the top and bottom of each unit cell. These copper sheets ensure that the only mode that is present at port 1 is the microstrip line mode. The VSWR (voltage standing wave ratio) at port 1 (microstrip port) is shown in Figure 3(b) for broadside radiation (red curve) and 60° scan in the E (blue curve), H (green curve), and D (black curve) planes. At broadside (red curve), the VSWR is below 2.6:1 from 14 GHz through 60 GHz. The impedance match remains near this value for scanning in the E and D planes. However, when scanning in the H-plane, there is a poor match since the VSWR increases to 4:1 at some frequencies.

The transmission coefficient from the microstrip line to the radiated field is shown in Figure 3(c). Both co- and cross-polarized radiation is shown for broadside radiation (red curve) and 60° scan in the E (blue curve), H (green curve), and D (black curve) planes. The cross polarization is below -15 dB for the broadside case, and when it is scanned in the E and H planes. Any cross polarization in these cases is due to unwanted radiation from the Marchand balun. The cross polarization is especially high when the array is scanned in the D-plane. This high cross polarization is a well-known limitation of Vivaldi arrays. The high cross polarization arises from the fact that as the radiated wave transitions from a guided transmission line mode to free space radiation, it encounters an anisotropic structure of Vivaldi elements. The situation is even worse when the length of the exponential taper is increased for wider bandwidth.

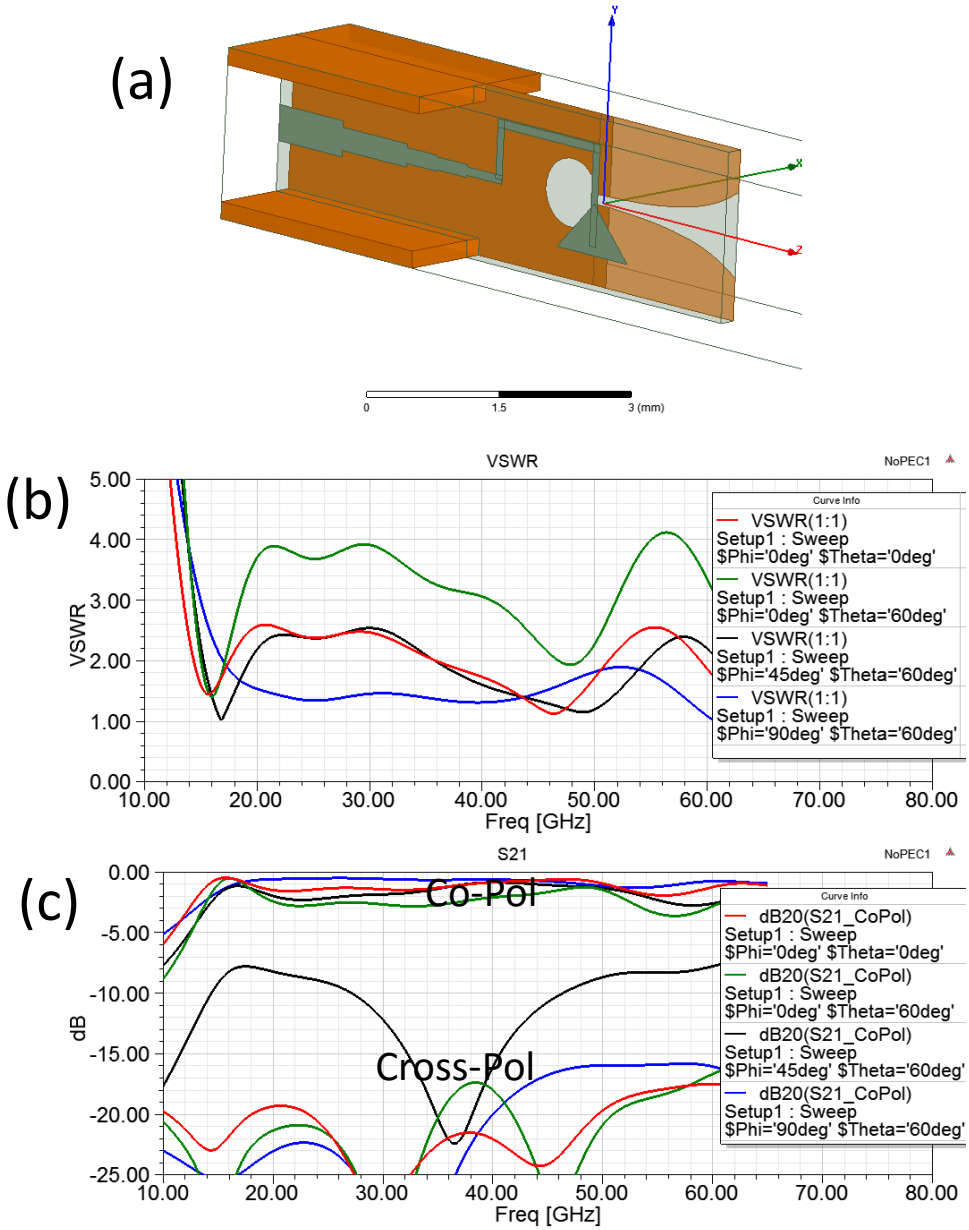

Figure 3: Geometry (a), VSWR (b), and Transmission (c) of the Vivaldi Array in Design 1

3.4.2 Design 2: Reduced Cross-Polarization Vivaldi Array

The cross-polarization can be improved by extending the copper sheets at the top and bottom of the unit cell in the $+z$-direction, as shown in Figure 4. These metallic sheets ensure that the radiating aperture is similar to a parallel plate waveguide, which exhibits a reasonable cross-

polarization when scanned to wide angles in arbitrary planes. The VSWR of this design is similar to the Design 1. However, the cross-polarization is noticeably improved. Again, the performance for broadside radiation (red curve) and 60° scan in the E (blue curve), H (green curve), and D (black curve) planes are shown. In this case, the cross-polarization for broadside radiation and scanning in the principal planes (i.e. E and H planes) is below -25 dB. The cross-polarization for scanning in the D-plane to $\theta = 60°$ is roughly -10 dB. As a point of reference, this cross-polarization level is identical that of a y-directed current sheet, which is a standard reference case.

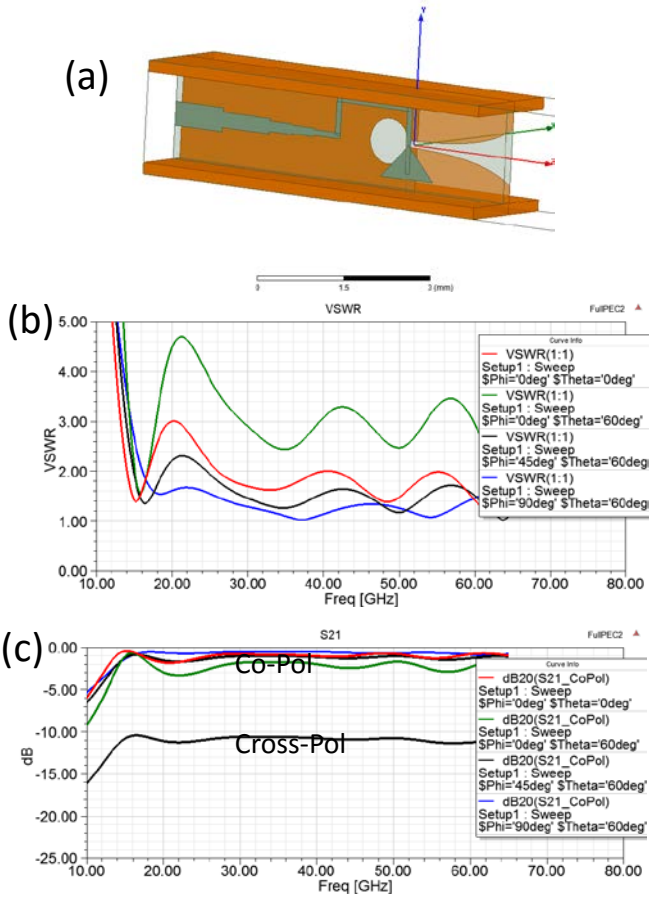

Figure 4: Geometry (a), VSWR (b), and Transmission (c) of the Reduced Cross Polarization Vivaldi Array

3.4.3 Design 3: Improved Scan Vivaldi Array

A common method of improving the performance of a phased array at wide scan angles is to place a dielectric slab on top of the array which acts as a wide angle impedance matching layer (WAIM) [12]. The dielectric slab acts as a shunt capacitor whose value is a function of the scan angle. This changing capacitance compensates for the different wave impedances seen at various scan angles. Here a 0.4 mm thick layer of Rogers 4003 ($\varepsilon = 3.55$) is placed on top of the aperture from Design 2, as shown in Figure 5. This dielectric layer improves the VSWR,

especially when scanning in the H-plane. Again, the performance for broadside radiation (red curve) and 60° scan in the E (blue curve), H (green curve), and D (black curve) planes are shown.

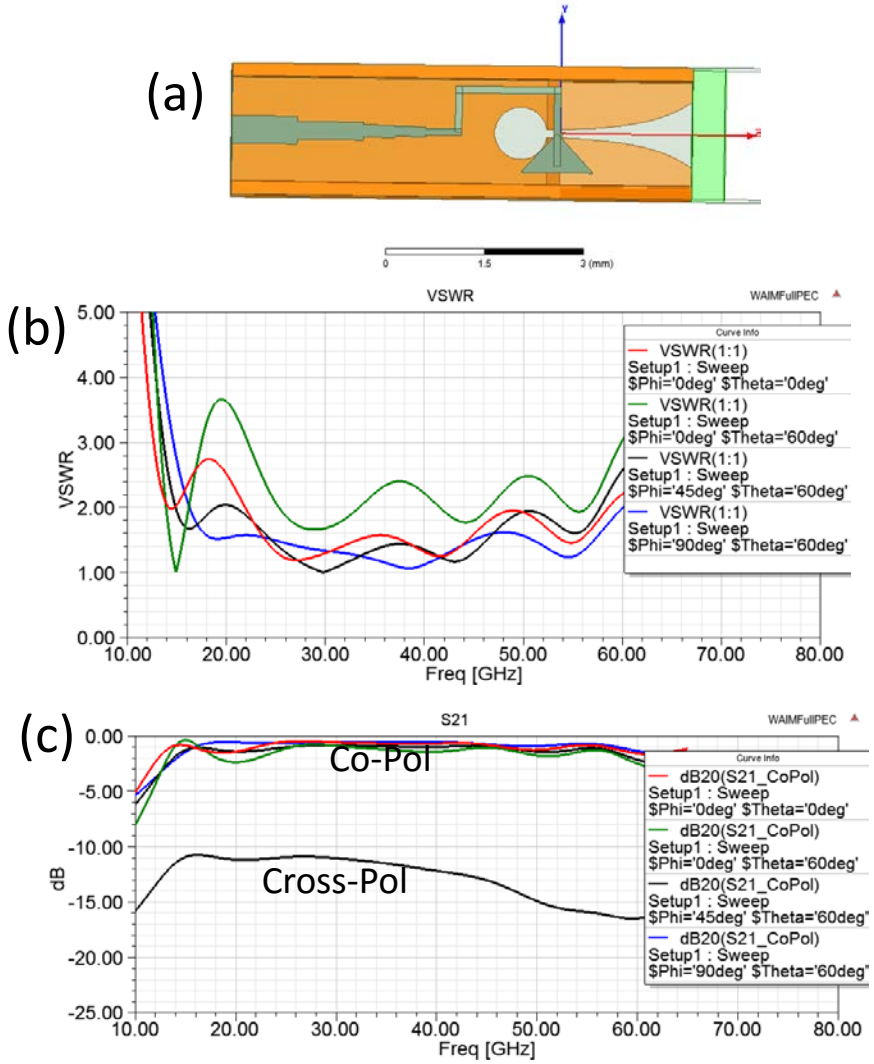

Figure 5: Geometry (a), VSWR (b), and Transmission (c) of the Improved Scan Vivaldi Array

3.4.4 Design 4: Simpler to Fabricate Vivaldi Array

The previous two designs used metallic sheets normal to the y-direction at the top and bottom of the unit cell to improve the cross polarization when scanning. These sheets were electrically connected to the ground plane in the yz plane. However, it can be challenging to electrically connect these two orthogonal boards using solder or conductive epoxy with a high reliability at small wavelengths. A more robust fabrication approach would be to replace the sheets with sub-

wavelength spaced, x-directed wires as shown in Figure 6. Since the wires are interwoven with the microstrip ground plane, there is no need for there to be an electrical connection. The VSWR and transmission coefficients using this approach are very similar to the previous case of using solid metallic sheets. Again, the performance for broadside radiation (red curve) and 60° scan in the E (blue curve), H (green curve), and D (black curve) planes are shown.

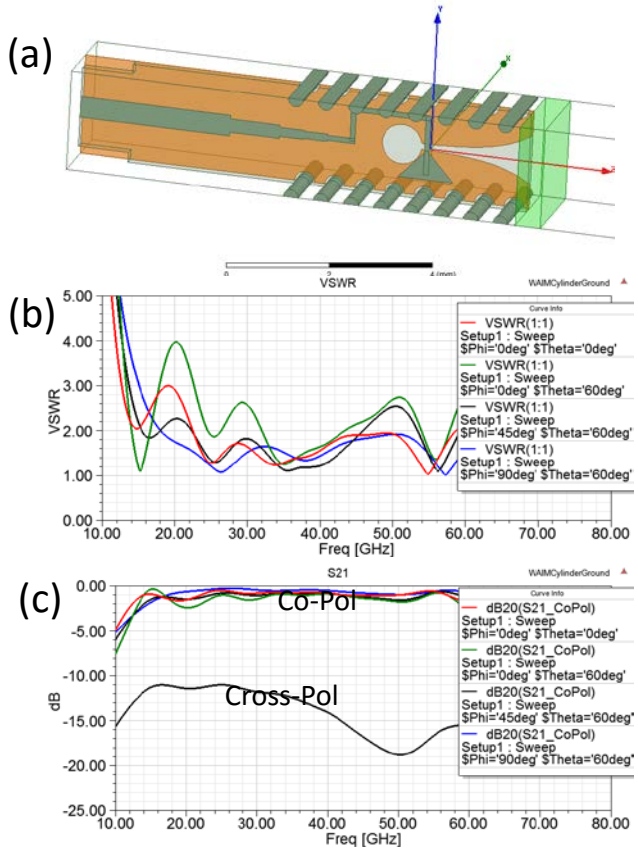

Figure 6: Geometry (a), VSWR (b), and Transmission (c) of the Simpler to Fabricate Vivaldi Array

3.4.5 Design 5: Vivaldi Array with Dielectric Matching Layers

Finally, dielectric matching layers are added to Design 3, as shown in Figure 7. In this design, 4 different dielectrics with permittivities 3.55, 2.2, 1.75, and 1.3 are placed on top of the aperture to provide a gradual impedance match to free space to improve VSWR. The thickness of the different layers are 0.5, 0.8, 1, and 1.5 mm, in order from highest permittivity to lowest, respectively. The thickness and permittivities were not optimized. In addition, the wave gradually bends toward the desired scan angle, which further reduces the cross polarization. There is no limit on the cross-polarization level that can be achieved with this approach. The VSWR and transmission coefficients are shown in Figure 7. Again, the performance for broadside radiation (red curve) and 60° scan in the E (blue curve), H (green curve), and D (black

curve) planes are shown. It should be noted that using dielectric matching layers can reduce the upper operating frequencies since the antenna can more easily couple to surface waves. Furthermore, dielectric matching layers are bulky since they add volume and weight to the array. It is also important to reduce air gaps between the different dielectric layers since these can generate reflections that deteriorate the performance. Another disadvantage of this approach is that the dielectric layers must have a larger area than the radiating aperture when the array is finite. Otherwise, there will be edge effects when the array is scanned to wide angles, which effectively reduces the aperture efficiency.

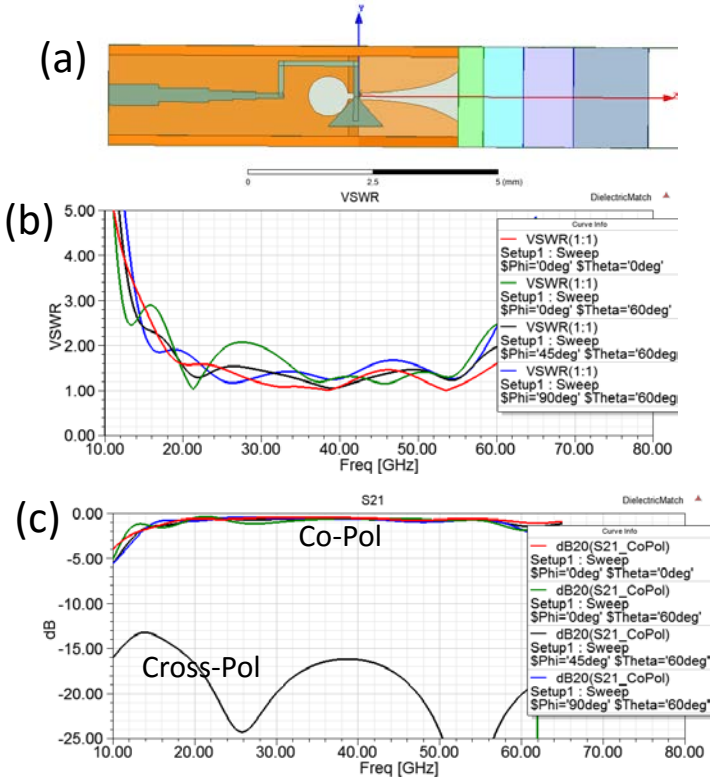

Figure 7: Geometry (a), VSWR (b), and Transmission (c) of the Vivaldi Array with Dielectric Matching Layers

3.5 Connected Dipole Array

The next linearly polarized array that is considered is the connected dipole array, which is shown in Figure 8. This array is also known as the current sheet array since strong mutual coupling between elements approximates a uniform sheet of radiating current with theoretically infinite bandwidth (when no ground plane is present) [8, 9]. In practice a ground plane is typically utilized to ensure the array radiates in the upper hemisphere. The presence of the ground plane reduces the bandwidth to several octaves if optimization is performed [13]. Connected dipole arrays are particularly attractive since they can provide a wide bandwidth while maintaining a low profile ($\lambda_h/4$ thickness) [14]. However, the presence of a ground plane can be problematic since the antenna can support even mode resonances that compromise performance [15].

A dipole array directly integrates a balun (typically Marchand balun) with the radiating dipoles [16]. A unit cell of the infinite array is shown in Figure 8 (a) and Figure 8 (b). The periodicity in the transverse plane is 2.5 mm x 2.5 mm. The dipole center is 1.75 mm above the ground plane. A bowtie dipole shape is used to improve bandwidth. A 0.4 mm thick Rogers 4003 substrate is placed on the dipole to act as a WAIM layer. The VSWR and transmission coefficients are shown in Figure 8 (c) and Figure 8 (d). The antenna has a narrower bandwidth than the Vivaldi array, but this could likely be improved with further optimization. The cross-polarization is close to that radiated by a *y*-directed current sheet. Again, the performance for broadside radiation (red curve) and 60° scan in the E (blue curve), H (green curve), and D (black curve) planes are shown.

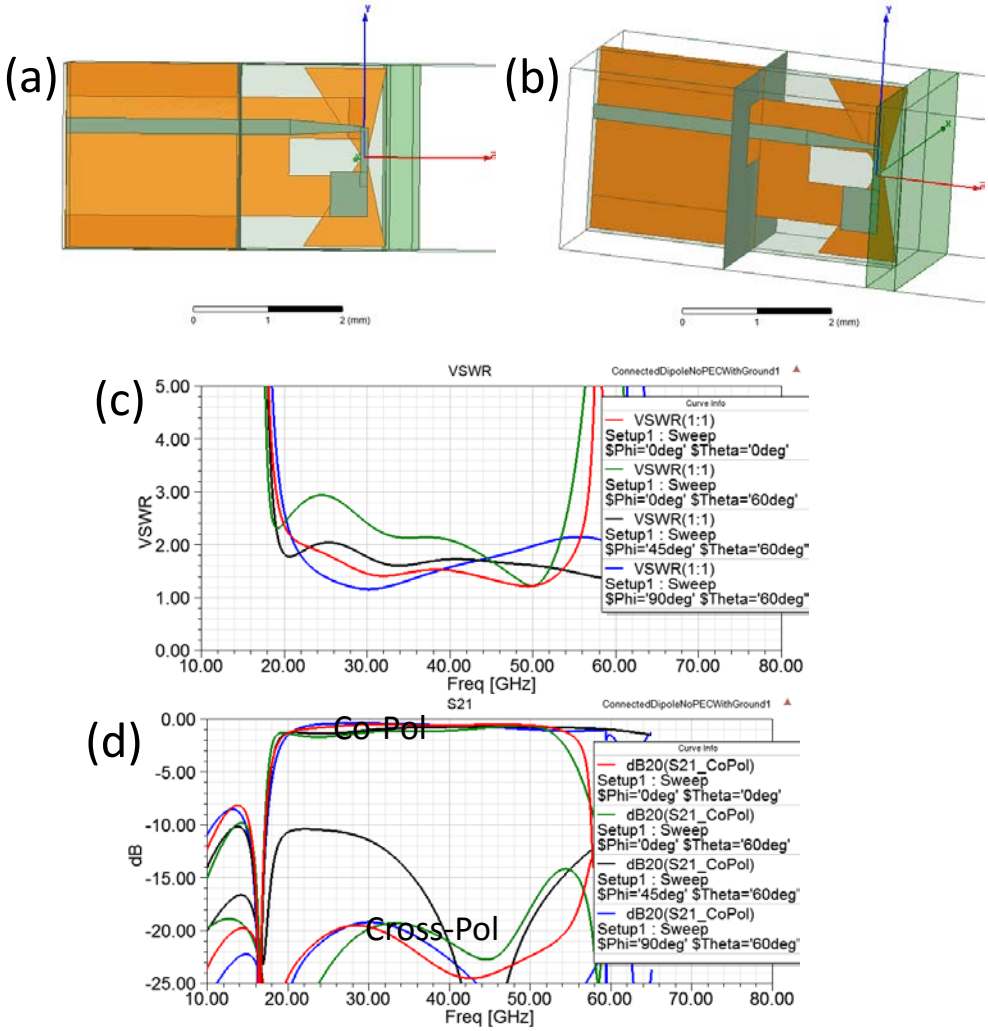

Figure 8: Geometry (a) and (b), VSWR (c), and Transmission (d) of the Connected Dipole Array

As mentioned, the connected dipole array can support even mode resonances if the metallic back-reflector is not connected to the microstrip trace's ground plane. It should be reiterated here that we are limiting ourselves to designs where the array is fed with PCBs oriented in the *yz* plane because this will eventually make it easier to integrate TR modules and cooling once they are developed. The primary purpose of the ground plane is to provide a strong back-reflector to

ensure the dipoles radiate in the $+z$ hemisphere. A slightly simpler geometry from a fabrication point of view is to utilize metallic plates (or wires) normal to the y-direction as shown in Figure 9. The metallic plates on the top and bottom of the unit cell ensure that the only propagating mode in the $-z$ direction is that of the microstrip line, which mimics the response of the metallic ground plane. Thus, the radiating dipole effectively sees a back-reflector. The VSWR and transmission coefficients for this geometry are shown in Figure 9 (b) and Figure 9 (c). The response is very similar to the previous case shown in Figure 8.

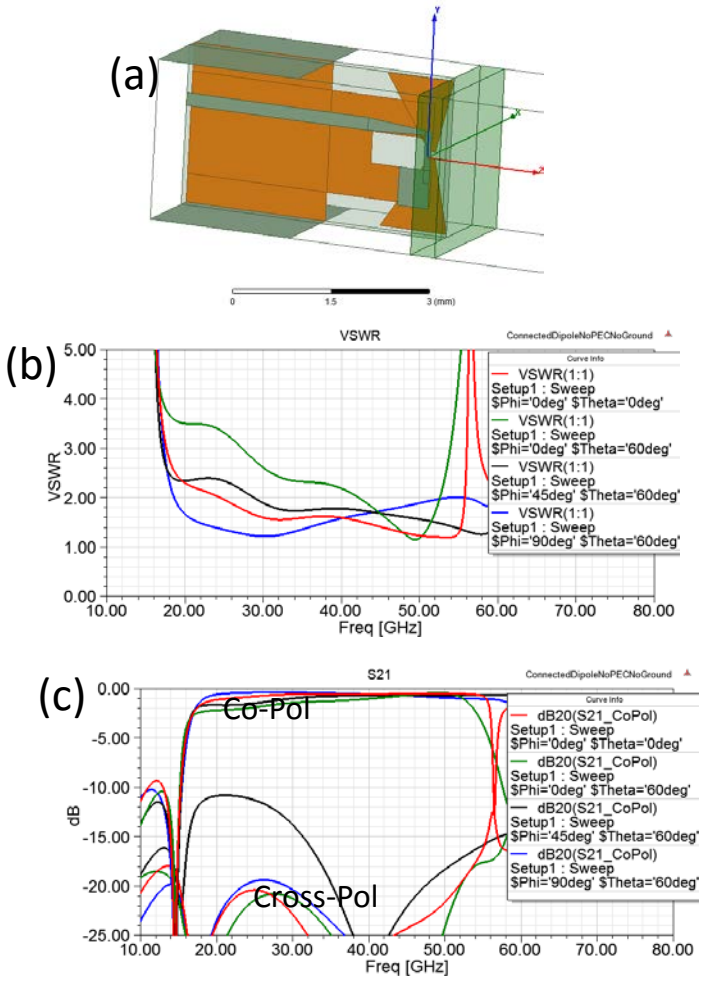

Figure 9: Geometry (a), VSWR (b), and Transmission (c) of the Simpler to Fabricate Connected Dipole Array

3.6 Summary

Broadband, linearly polarized phased arrays are reviewed. It is shown that both Vivaldi elements and connected dipoles can operate over the desired frequency range of 20 to 60 GHz. There are many similarities between the two arrays. In both cases, a broad bandwidth is realized by tightly coupling adjacent unit cells. In addition, the performance at wide scan angles is improved by integrating a WAIM layer on top of the radiating elements. Placing metallic walls in the direction

orthogonal to the radiated polarization improves polarization purity. It is expected that the performance of all these arrays could be improved with optimization.

The Vivaldi array is advantageous since they are more robust to fabrication tolerances, and its bandwidth can be easily controlled by changing the length of the exponential taper. Vivaldi arrays are typically thicker than a connected dipole arrays. However, the notable thickness is not a big concern for our application due to the small operating wavelengths. Therefore, the remainder of this report will focus on Vivaldi arrays.

4.0 Approach 1: Dual-Polarized Antenna Fed with 90° Hybrid

4.1 Introduction

In this section, the design approach shown in Figure 10 is considered for generating circular polarization. A TR module for each element in the array feeds a 90° hybrid coupler, which then excites a broadband, dual-linear polarized antenna. This approach is a more conventional method of realizing a circularly-polarized array due to its systematic design procedure. Each component of this system (90° hybrids, baluns, and dual-polarized antennas) is a proven technology, which initially suggests that this is a promising approach. However, it is shown here that it is actually quite challenging to combine all of these components together to realize a broadband, circularly polarized phased array that can electronically scan to different angles.

First, different circularly polarized antennas are quickly discussed, and the dual-polarized Vivaldi is determined to be the most promising for our application. Next, it is noted that the conventional egg-crate array that is typically utilized for radiating dual-linear polarizations has offset phase centers for the vertical and horizontal polarizations. Therefore, these arrays cannot be connected to a 90° hybrid and radiate circular polarization at different scan angles. Next, dual-polarized antennas with co-located phase centers are considered. It is shown that these antennas support even mode resonances that must be properly dissipated, which adds complexity. Finally, it is noted that even if it is possible to design a perfectly working Vivaldi array with co-located phase centers, there would likely be significant fabrication issues.

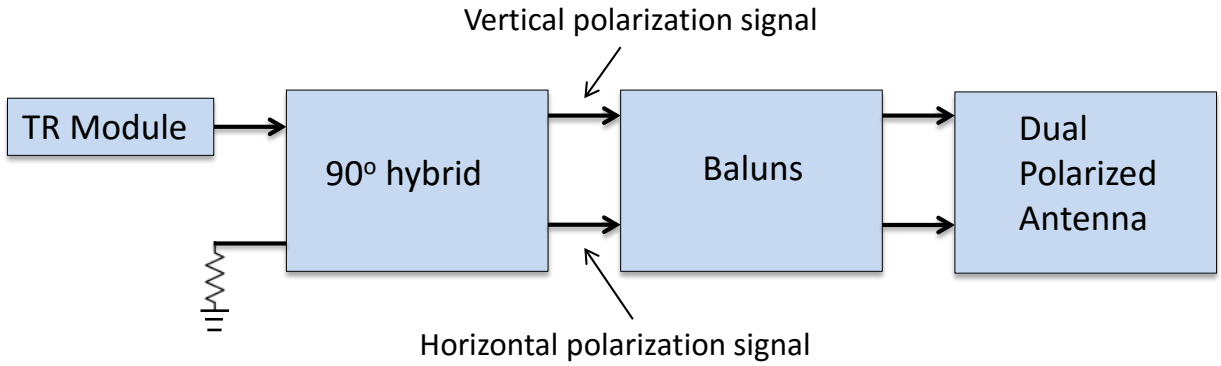

Figure 10: Architecture Where the Signal from a TR Module Feeds a 90° Hybrid Coupler, 2 Baluns for Vertical and Horizontal Polarizations, and is Then Radiated by a Dual-Linear Polarized Antenna

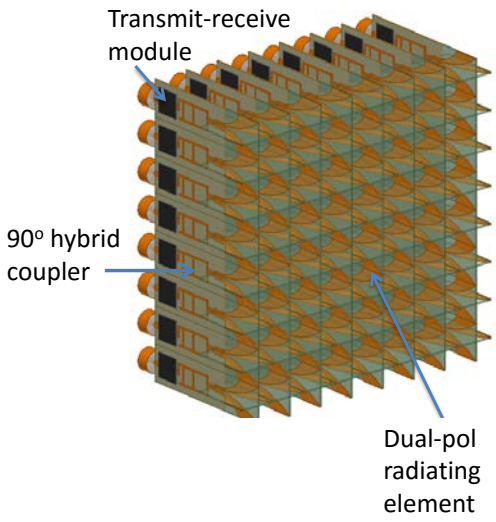

Figure 11: Generic Geometry of a Dual-Linear Polarized Array Integrated with TR Modules Radiates Circular polarization

4.2 Circularly Polarized Antennas

The first step in designing a circularly polarized array is to choose a radiating element. A planar spiral antenna is self-complementary, which allows it to radiate circular polarization with many octaves of bandwidth [17]. However, this antenna is typically multiple wavelengths in diameter at the upper operating frequencies, which makes it unsuitable for wide angle scanning since an array with $\lambda/2$ spacing is unrealizable. Furthermore, the bandwidth is dramatically reduced once a ground plane is placed behind the spiral to remove radiation in the lower half plane. A helix antenna that winds a wire out of the plane has a smaller diameter than a planar spiral antenna [17]. However, its diameter is still too large to allow for wide scanning over a 3:1 bandwidth. In addition, they have poor scan performance because of strong coupling due to long lengths in the axial direction. In fact, there are not any antennas that we are aware of that directly radiate circular polarization with octaves of bandwidth, and can also be arrayed with $\lambda/2$ spacing for wide angle scanning.

It is also possible to generate circular polarization using dual-linear polarized antennas, and feeding them in phase quadrature with a $90°$ hybrid coupler. This is the approach that will be taken here since dual-linearly polarized antenna arrays and $90°$ hybrid couplers with octaves of bandwidth are proven technologies [1] [3] [18].

4.3 Egg Crate Array Limitations

Let us consider the dual polarized radiating element. Vivaldi arrays, connected dipoles, and connected slot arrays can all satisfy the bandwidth requirements [2]. Vivaldi arrays are considered here due to their simplicity. The elements in these arrays are typically arranged in an egg-crate geometry as shown in Figure 12. This approach is attractive because the vertical and horizontal polarizations are displaced from each other, which increases isolation. Therefore, the performance of the dual-polarized array is very close to that of a single polarized array.

However, this approach is problematic for our application for several reasons. First of all, each element would need to be fed with a connector. The spacing between horizontal and vertical connectors needs to be 1.75 mm to ensure $\lambda_h/2$ spacing, where λ_h is the wavelength at the highest operating frequency (60 GHz here). However, this spacing is too small to fit connectors at each element since the smallest commercially available connector (G4P0) requires a minimum pitch of 2.25 mm. In addition, this approach would be expensive since each connector is on the order of $50.

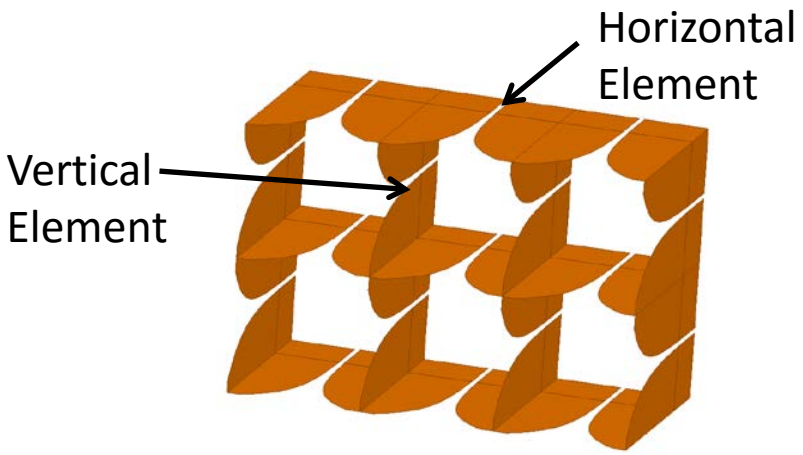

Figure 12: Egg-Crate Array of a Dual-Polarized Vivaldi Antennas

Even if smaller connectors are manufactured, the egg-crate array requires unique phase shifters for the vertical and horizontal elements, which effectively doubles the required number of TR modules. In other words, it cannot be fed with a 90° hybrid and be expected to operate at wide scan angles. The reason for this is the horizontal radiators have phase centers that are displaced by $\lambda_h/4$ in both the x and y directions from the vertical elements, which generates high cross circular polarization. For example, if a 90° hybrid were used to feed each element, the axial ratio of the transmitted beam would degrade from 0 dB at broadside to 12 dB at 45^o scan angles at the upper operating frequency.

It should be noted that it may possible to use a modified egg crate array that compensates for the displaced phase centers of vertical and horizontal polarizations. If the array is arranged as shown in Figure 13, the phase centers of the vertical and horizontal elements are collocated [19]. A single vertical polarization signal trace would need to be split using a Wilkinson power divider to feed the two radiating ports. The same argument applies for the horizontal polarization as well. In total, this approach would require 4 baluns, and 2 Wilkinson power dividers for each unit cell, which would likely be difficult to accurately fabricate at mm-wave frequencies.

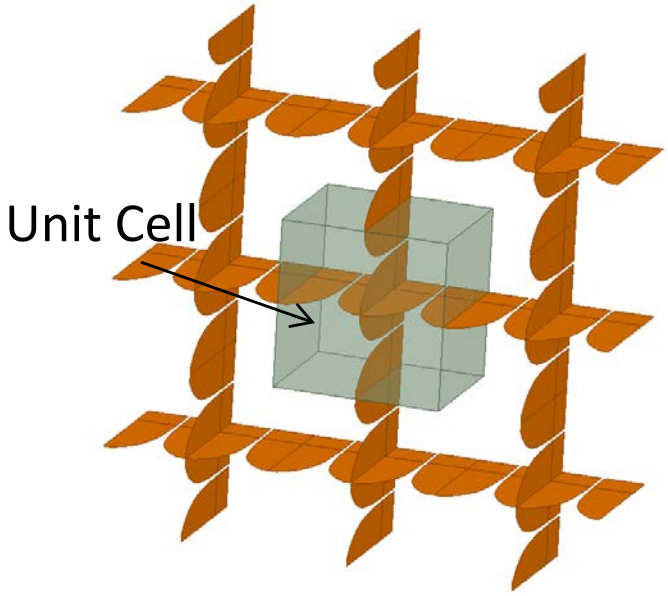

Figure 13: Array of Vivaldi Elements Assembled in a Modified Egg-Crate Geometry that Provides Co-Located Phase Centers for Vertical and Horizontal Polarizations

4.4 Dual Polarized Radiator with Co-Located Phase Centers

Due to the limitations of the egg-crate geometry, dual-polarized antennas with co-located phase centers between vertical and horizontal polarizations are considered. The basic antenna geometry is shown in Figure 14. For simplicity, let us first characterize the antenna assuming it is ideally fed with balanced strips. There is PEC on the sides of the unit cell in the region $z < 0$, which ensures that each cell is isolated from its neighbors in this region. The transmission coefficient of this array when directed towards broadside is shown in Figure 15. The array is well matched to free space from 20 GHz to 60 GHz.

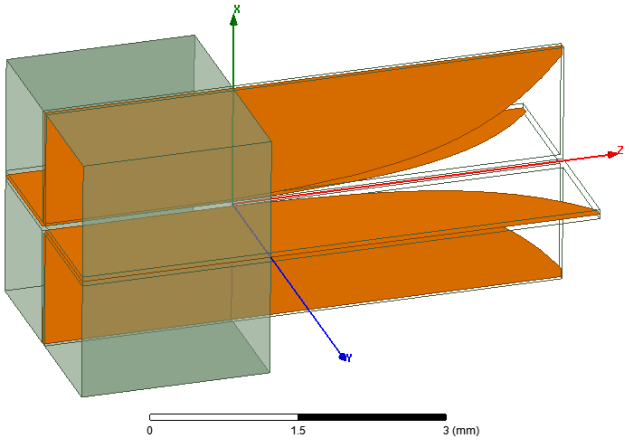

Figure 14: Dual polarized Vivaldi Antenna with Co-Located Phase Centers

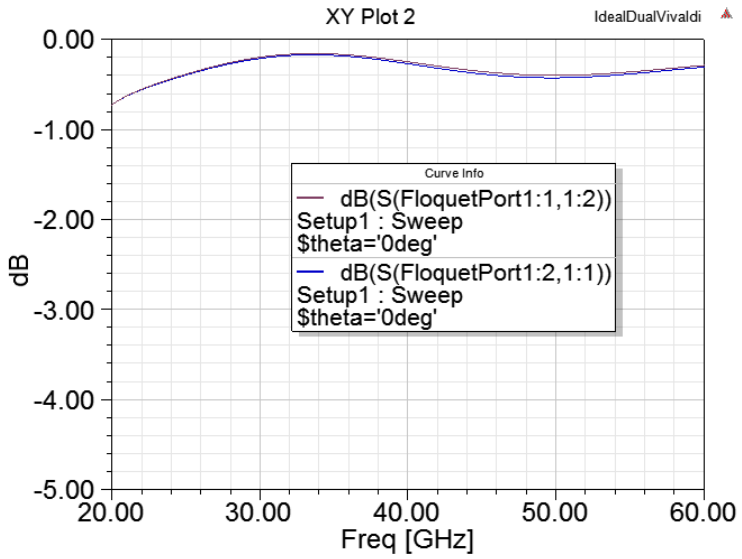

Figure 15: Transmission Coefficient from the Vertical and Horizontal Polarizations of the Vivaldi Element to Free space Radiation When the Antenna is Directed Towards Broadside

Since the vertical and horizontal polarizations are near each other at the feed, there are three modes supported by this geometry, as shown in Figure 16. The first two modes are differential modes, which excite the Vivaldi elements such that the vertical and horizontal polarizations are efficiently radiated. However, there is also an undesired even mode that does not radiate well. The presence of this even mode does not affect the performance when the antenna radiates towards broadside since coupling from the differential modes to the even mode is insignificant due to symmetry. However, when the antenna is scanned to oblique angles, the even mode is coupled to the odd modes. For example, Figure 17 shows coupling between the three modes when the antenna is scanned to $\theta = 50°$, $\phi = 0°$. There is relatively strong coupling between the vertical odd mode and the even mode. Let us consider what happens when the presence of this even mode is neglected in the design process, and the vertical and horizontal polarizations are simply fed using two baluns. In this case, the even mode would be effectively terminated with a short circuit at the balun. The transmission coefficients from the differential modes to free space contain undesired resonances, as shown in Figure 18. If the even mode is instead terminated with a matched load, its presence does not generate resonances. Instead, the presence of the even mode only reduces the radiation efficiency at wide scan angles, as shown in Figure 19.

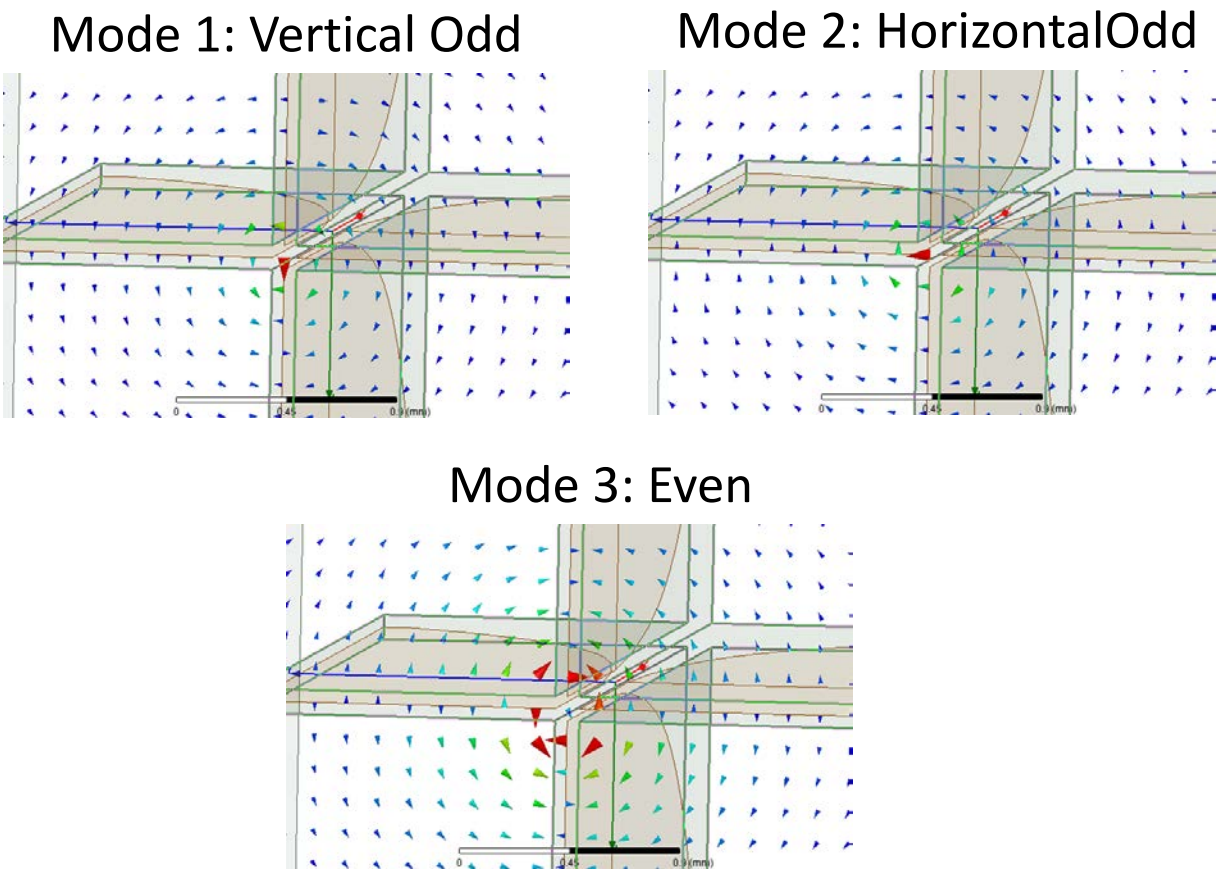

Figure 16: Three Different Modes Supported by the Dual-Linear Polarized Vivaldi Antenna

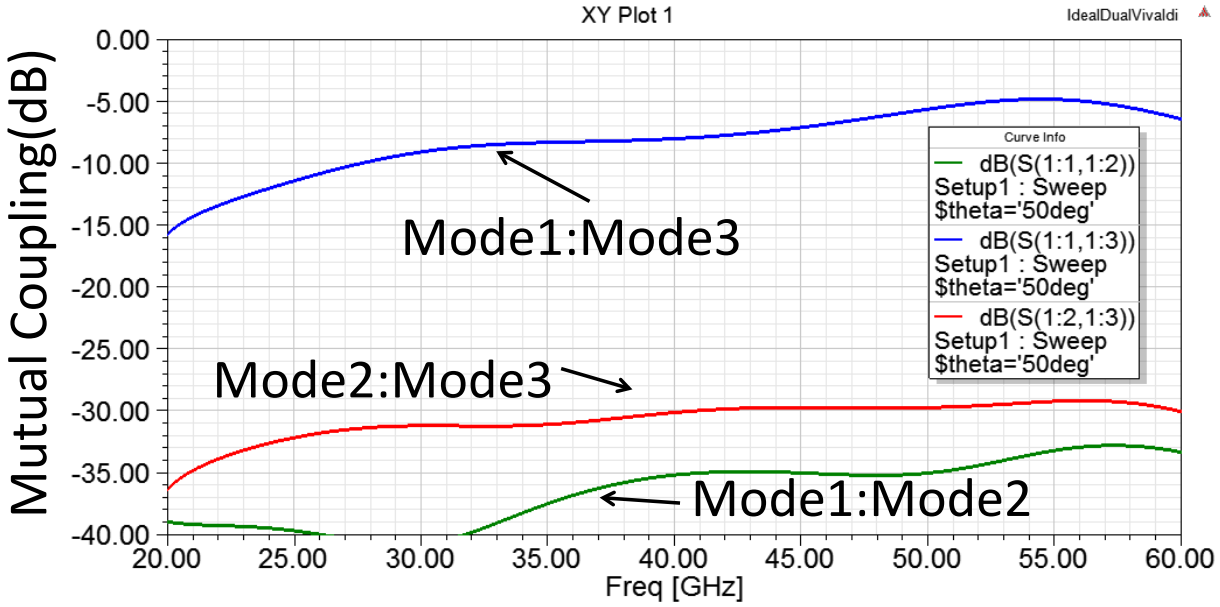

Figure 17: Coupling Between the Three Different Modes Supported by the Dual-Polarized Vivaldi Element When the Array is Scanned to $50°$ *in the Vertical Plane (*xz *plane)*

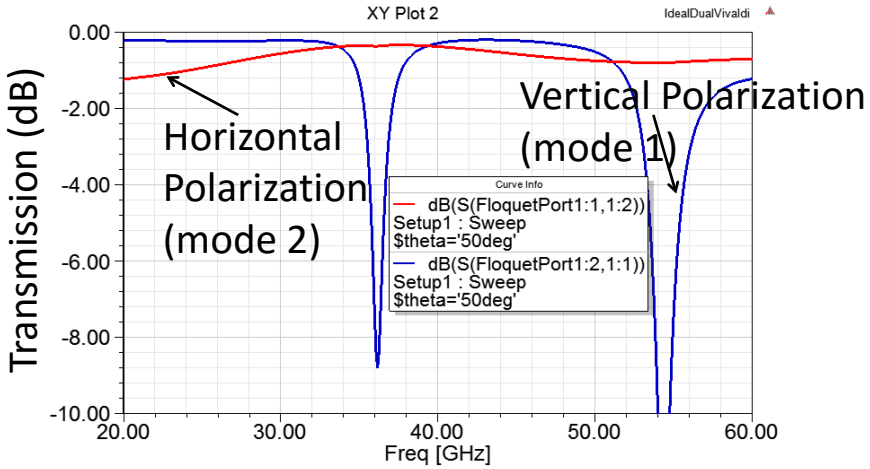

Figure 18: Transmission Coefficients When the Antenna is Scanned to $50°$ *in the (*xz *plane) and the Even Mode is Terminated with a 1* Ω *Resistance*

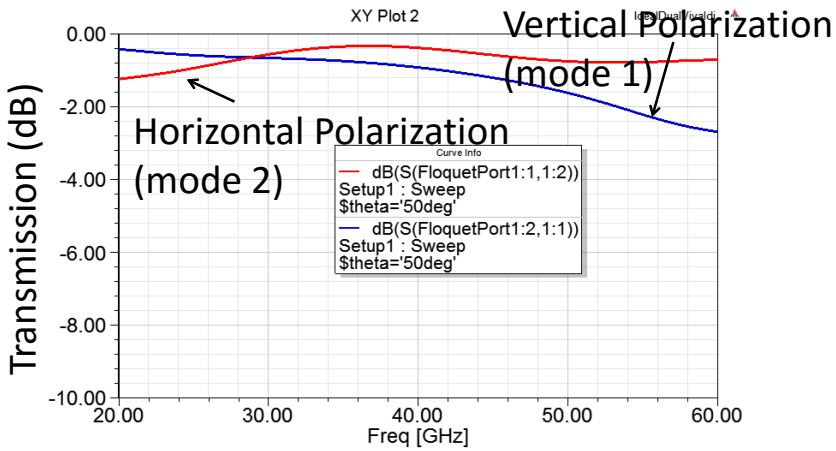

Figure 19: Transmission Coefficients When the Antenna is Scanned to 50° *in the (*xz *plane) and the Even Mode is Terminated with its Port Impedance*

4.5 Examples

A more concrete example of the challenges associated with realizing a wideband, dual-pol antenna with co-located phase centers is shown in Figure 20. It should be emphasized that although the examples below are not optimized, they do provide insight into the issues associated with this type of antenna. This geometry does not utilize any resistive loading to terminate the unwanted even mode when the beam is scanned from broadside. Therefore, we expect to see resonances throughout the band. The dual-polarized antenna is fed with two stripline waveguides to feed the vertical and horizontal polarizations. Baluns that convert the stripline mode to a balanced differential mode are also integrated into the design. The transmission efficiency ($|S_{21}|^2$) of the two different polarizations when scanned to 50^o in a principal plane is shown in Figure 21. The blue curve (E-plane scan) has many unwanted resonances throughout the band due to common mode resonances.

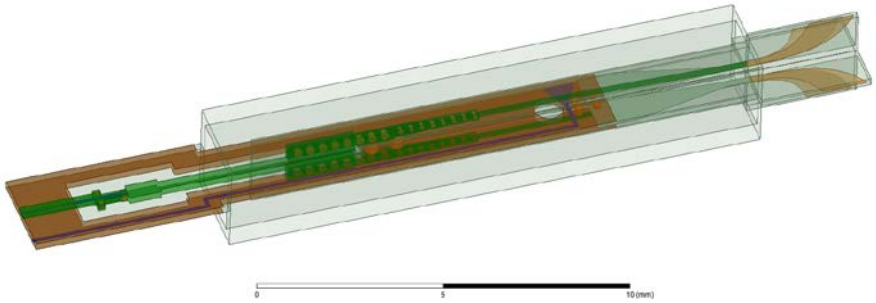

Figure 20: Unit Cell of a Dual-Linear Polarized Vivaldi Array Fed by Two Stripline Waveguides

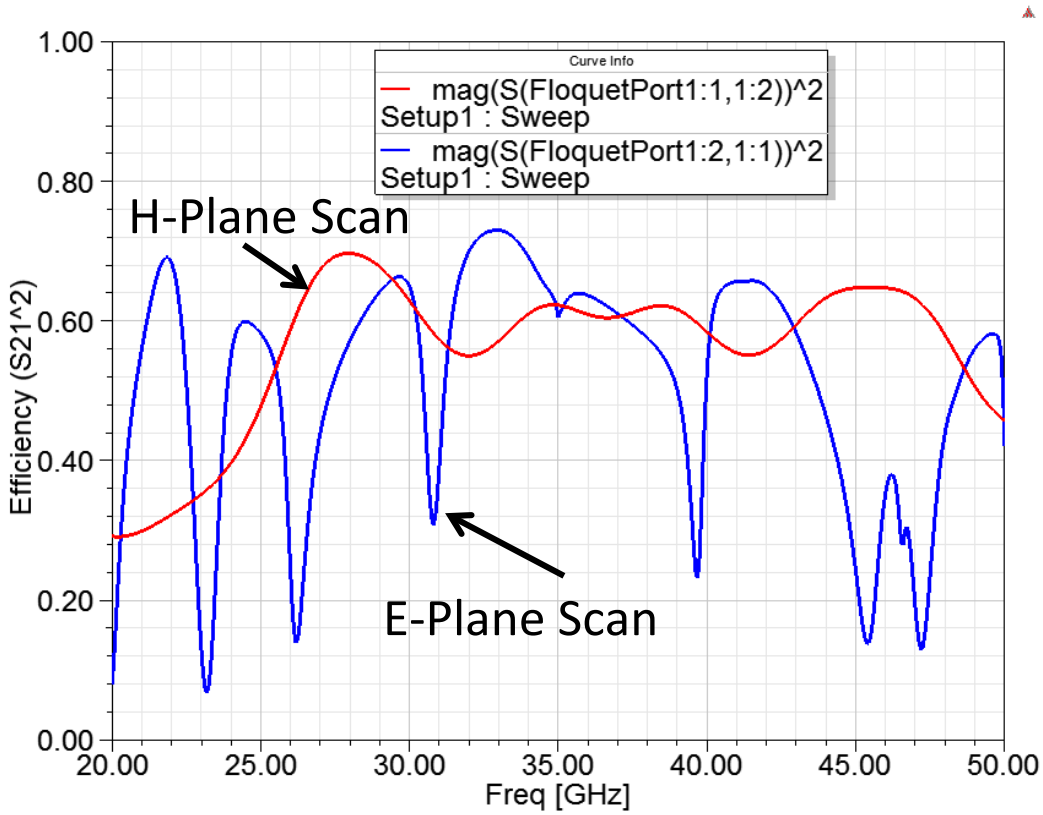

Figure 21: Transmission Efficiency ($|S_{21}|^2$) from the Stripline Modes to Plane Wave Modes of the Unit Cell Shown in Figure 20 When the Array is Scanned to 50° *in a Principal Plane*

There are different methods of dissipating energy in the even modes to remove unwanted resonances throughout the band. The most straightforward method would be to simply add additional power dividers and baluns. However, the spacing between signal traces is already tight if we limit ourselves to minimum feature sizes that are on the order of 0.1 mm within a unit cell that is 2 mm in size. Therefore, it is difficult to fit additional power dividers and baluns within a unit cell. To demonstrate that it is theoretically possible to dissipate even mode resonances, another unit cell is designed which integrates resistive loads into the structure (see Figure 22). The transmission coefficient of this unit cell is shown in Figure 23, when it is scanned to 50° in a principal plane. It can be seen that the resonances throughout the band are significantly reduced. It should be noted that the transmission coefficient is below 50% for most of the band, which is quite low. This low efficiency could likely be improved with optimization since this structure was not systematically designed. There is also significant impedance mismatch in this design, which could likely be improved with additional effort.

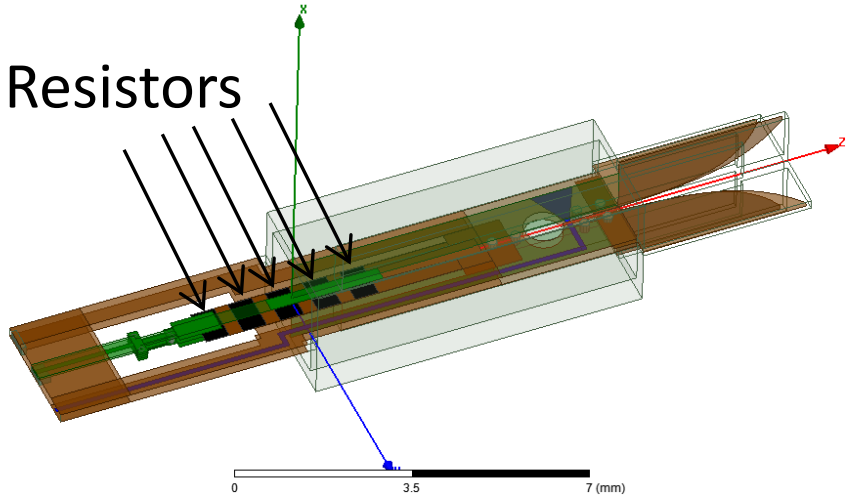

Figure 22: Unit Cell of a Modified, Vivaldi array That Dissipates Reflection Into the Even Mode Using 5 Resistors

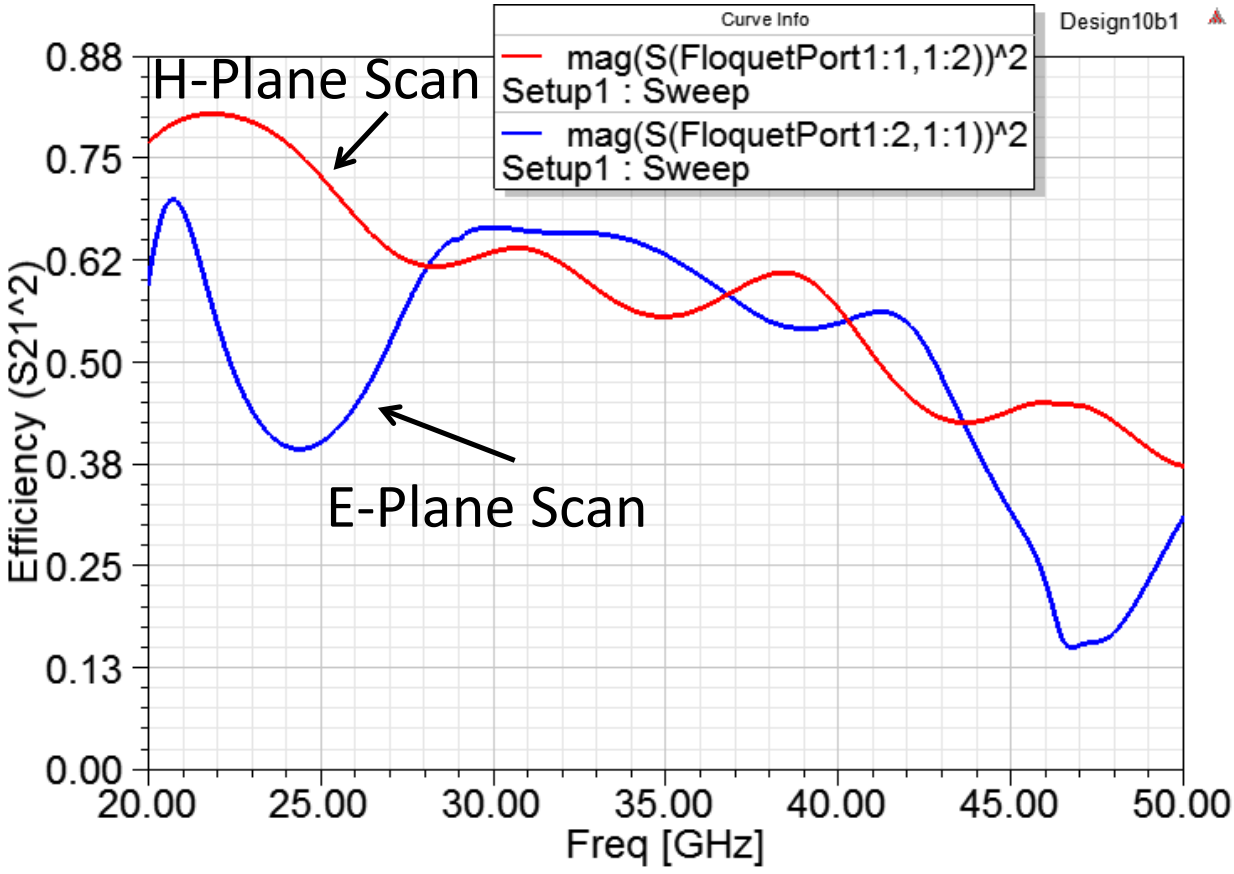

Figure 23: Transmission Coefficient of the Modified Vivaldi Array that Incorporates Resistors to Dissipate Reflection into the Even Mode

4.6 Outstanding Issues and Summary

It should also be reiterated that the basic approach discussed in this section feeds each element with a planar PCB as shown in Figure 11. If a dual-polarized antenna is used, some method of guiding signals from a PCB to an orthogonally oriented PCB must be used so that both vertical and horizontal polarizations can be radiated. This type of transition typically relies on connectors. However, as mentioned earlier, there is not enough space to fit the smallest commercially available connectors. In addition, connectors would be expensive. Alternatively, it may be possible to connect orthogonal PCBs together by simply bringing traces on the two boards next to each other and electrically connect them using solder or conductive epoxy. This is the approach that was considered in Figure 20 and Figure 22. However, soldering two orthogonal circuit boards together is a nonstandard fabrication process that would require development at mm-wave frequencies. It is unclear how good of a connection can be achieved using this method.

It should also be noted that the 90^{o} hybrid coupler for feeding the vertical and horizontal polarizations was not investigated in detail due to time constraints. It is our opinion that realizing this coupler should be straightforward since offset stripline couplers with multiple octaves of bandwidth and insertion losses ~1 dB are commercially available at mm-wave frequencies [18].

In summary, it is quite challenging to realize a phased array that directly radiates circular polarization at mm-wave frequencies. It should also be noted that two practical assumptions have been made to account for the current technology status as we see it:

1) The array should be fed with planar PCBs as shown in Figure 11, which is necessary to provide sufficient area for the TR modules and cooling.
2) The minimum feature size in all of the designs should be around 0.1 mm to remain compatible with standard PCB fabrication techniques.

These assumptions immediately place constraints on the antenna design options. Due to the many design challenges highlighted in this section, the approach shown in Figure 10 was abandoned. Instead, we focused our efforts on combining a linearly-polarized array with a linear-to-circular polarizer.

5.0 Approach 2: Linear-to-Circular Polarizer Placed on a Linearly Polarized Array

5.1 Introduction

As discussed in previous sections, it is extremely difficult to implement a wide-band feed for exciting a circularly polarized array at the mm-wave band. This approach would require complex structures in a very limited space. Furthermore, the complexity in integrating TR modules and cooling channels suggests that the whole structure is practically impossible to fabricate outside of a clean room. The next architecture that was considered is shown in Figure 24. In this architecture, the complexity is functionally divided divided into two areas: the linearly polarized feed and linear-to-circular polarizer. In this fashion, the simpler feed allows integration of TR modules and cooling systems, while circular polarization is generated with multi-layer structures on top of the radiating aperture, as shown in Figure 25. This architecture is advantageous since a linearly polarized antenna is a natural geometry if the feed consists of planar PCBs. However, the linear-to-circular polarizer requires unprecedented performance in terms of both bandwidth and scan angle. Therefore, this entire section is devoted to the polarizer design. It should be noted that the linear-to-circular polarizer in this architecture accomplishes the same function as the 90° hybrid coupler in the previous architecture. A disadvantage of using a linear-to-circular polarizer is it must work for a wide range of incident angles, whereas the performance of the 90° hybrid is independent of the scan angle. An advantage of this geometry is it is more modular since the linear-to-circular polarizer can be added or removed from the array as needed. The simulation and measurement results presented in this section show it is possible to fabricate high-performance linear-to-circular polarizers, which suggest that this approach is the most promising method for realizing a circularly polarized phased array at mm-wave frequencies.

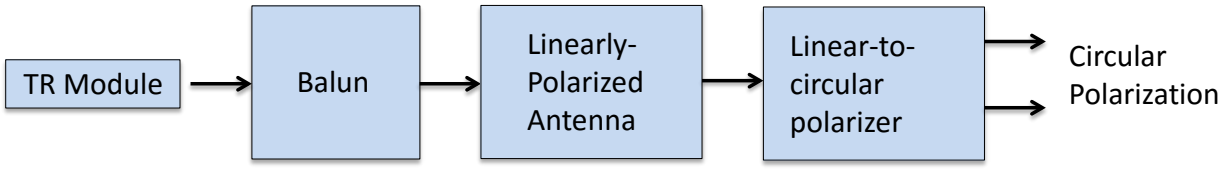

Figure 24: Architecture Where the Signal from a TR Module is Radiated by a Linearly Polarized Antenna, and is Converted to Circular Polarization by a Linear-to-Circular Polarizer

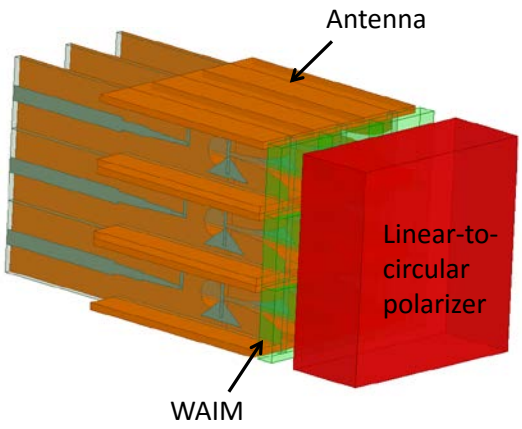

Figure 25: A More Physical Representation of the Balun, Antenna, and Polarizer that is Shown in Figure 24

5.2 Previous Work

Linear-to-circular polarizers convert an incident, linearly polarized plane wave into a transmitted, circularly polarized wave. Linear-to-circular polarizers are commonly utilized from microwave to optical frequencies for a myriad of applications. Many of these applications also demand wide operating bandwidths and wide angles of incidence. However, conventional linear-to-circular polarizers only work perfectly at a single frequency, which make them inherently narrowband. This fact has inspired significant research efforts to extend their bandwidth.

At THz frequencies and higher, wideband linear-to-circular polarizers are typically realized by cascading multiple birefringent waveplates with rotated principal axes [20, 21, 22]. Polarizers utilizing cascaded waveplates can realize multiple octaves of bandwidth. At these higher frequencies, the geometry can afford to be many wavelengths in thickness while still maintaining a low profile since the wavelength is small. A disadvantage of previous designs is they do not typically work well at wide angles of incidence since the optical thickness of each layer is a function of the angle of incidence.

At microwave frequencies, the most common linear-to-circular polarizers utilize cascaded patterned metallic sheets (i.e., sheet impedances) with subwavelength overall thicknesses [23, 24]. The bandwidth of microwave linear-to-circular polarizers frequencies are typically less than 40%. In some examples, the bandwidth has been increased up to an octave using meanderline metallic patterns printed on dielectric substrates [25, 26]. However, these meanderline polarizers do not typically work well at wide angles of incidence when their bandwidth is large [27].

Here, we aim to develop linear-to-circular polarizers at mm-wave frequencies that realize multiple octaves of bandwidth and operate at wide scan angles. Approaches inspired by both optics and microwave engineering communities are considered. First, an approach inspired by

the optics community is used, where the polarizer consists of cascaded waveplates. Rather than utilizing naturally occurring materials, each waveplate is realized with artificial anisotropic dielectrics. The polarizer is designed to work at significantly wider angles of incidence than the state-of-the-art by engineering the permittivity in the x, y, and z directions. Next, a polarizer inspired by the microwave engineering community is reported, which consists of cascaded sheet impedances. In contrast to previous designs, the polarizer utilizes metallic patterns shaped as both meanderline and patch geometries. Furthermore, the principal axes of each sheet are rotated by optimized angles to increase the degrees of freedom and performance. This cascaded sheet impedance polarizer is easier to fabricate and thinner than the cascaded waveplate polarizer. Both polarizers are designed using a genetic algorithm optimization process, and their simulated and measured performances are reported. Finally, it is shown that it is possible to refine the performance of a fabricated prototype by quickly 3D printing a dielectric grating that compensates for fabrication tolerances.

5.3 Definitions

It is useful to define some metrics used to characterize the performance of linear-to-circular polarizers. Consider an arbitrary structure illuminated with a normally incident plane wave. The linearly polarized transmission matrix ($\boldsymbol{T}^{LIN}$) of the structure relates the incident electric field E_i to the transmitted electric field E_t,

$$\begin{pmatrix} E_t^x \\ E_t^y \end{pmatrix} = \boldsymbol{T}^{LIN} \begin{pmatrix} E_i^x \\ E_i^y \end{pmatrix} = e^{-j\delta} \begin{pmatrix} T_{xx} & T_{xy} \\ T_{yx} & T_{yy} \end{pmatrix} \begin{pmatrix} E_i^x \\ E_i^y \end{pmatrix} \tag{3}$$

where δ is an unimportant phase shift. Without loss of generality, an ideal linear-to-circular polarizer converts an incident x-polarization to a transmitted right-handed circular polarization. In other words, $T_{xx} = 1/\sqrt{2}$ and $T_{yx} = -\mathrm{j}/\sqrt{2}$. It is often more convenient to characterize the performance of a linear-to-circular polarizer by considering the linear-to-circular transmission matrix ($\boldsymbol{T}^{CP}$) which is defined here as,

$$\begin{pmatrix} E_t^R \\ E_t^L \end{pmatrix} = \boldsymbol{T}^{CP} \begin{pmatrix} E_i^x \\ E_i^y \end{pmatrix} = \begin{pmatrix} T_{Rx} & T_{Ry} \\ T_{Lx} & T_{Ly} \end{pmatrix} \begin{pmatrix} E_i^x \\ E_i^y \end{pmatrix}, \tag{4}$$

where R and L denote transmission into right and left handed circular polarizations, respectively. $\boldsymbol{T}^{CP}$ is related to $\boldsymbol{T}^{LIN}$ by,

$$\boldsymbol{T}^{CP} = \sqrt{2} \begin{pmatrix} 1 & 1 \\ -j & j \end{pmatrix}^{-1} \boldsymbol{T}^{LIN} \tag{5}$$

Ideally, $T_{Rx} = 1$ and $T_{Lx} = 0$. The polarization purity of the transmitted wave is often expressed in terms of the axial ratio (AR), which can be related to the linear-to-circular transmission matrix by,

$$AR = \frac{|T_{Rx}/T_{Lx}| + 1}{|T_{Rx}/T_{Lx}| - 1}. \tag{6}$$

Note that a y-polarized incident wave is not considered here.

The polarizers reported here are characterized at different angles of incidence. The E and H planes are defined relative to the plane of the incident wave. In other words, the E-plane corresponds to the $\phi = 0°$ plane and the H-plane is the $\phi = 90°$ plane. It should also be noted that the term T_{Rx} is used to characterize transmission of obliquely incident waves as well as normally incident waves. Rigorously speaking, the incident polarization is x-polarized with respect to the third-definition provided by Ludwig [10].

5.4 Design and Simulation

5.4.1 Cascaded Waveplate Polarizer

Conventional waveplates composed of uniaxial dielectrics (i.e., $\varepsilon_{xx} = \varepsilon_{zz} \neq \varepsilon_{yy}$) only operate at a single frequency. It has been known since the 1950's that the bandwidth can be significantly extended by cascading waveplates with different thicknesses and relative orientations to develop so-called achromatic waveplates [20]. These waveplates are commercially available at optical frequencies with bandwidths of over 4:1 [28]. This design approach has been scaled down from optical frequencies to THz [21] and mm-waves [22]. However, as the wavelength is increased further, the required thickness of naturally occurring crystals becomes prohibitive due to the notable, weight, size, and loss. Therefore artificial anisotropic dielectrics (i.e., metamaterials), are considered here.

To begin, let us analyze the simplest linear-to-circular polarizer, which is a single waveplate. Ignoring reflection losses and absorption for the moment, the transmission matrix of a waveplate can be written as,

$$\boldsymbol{T}_{wp}(\beta, d\Delta n) = \boldsymbol{R}(\beta)^{-1} \begin{pmatrix} 1 & 0 \\ 0 & e^{-jk_0 d\Delta n} \end{pmatrix} \boldsymbol{R}(\beta), \tag{7}$$

where $k_0 = \omega\sqrt{\varepsilon_0 \mu_0}$ is the wave impedance of free space, d is the thickness of the waveplate, Δn is the difference in refrefractive index along the two principal axes and $\boldsymbol{R} = \begin{pmatrix} \cos(\beta) & -\sin(\beta) \\ \sin(\beta) & \cos(\beta) \end{pmatrix}$ is the β-degree rotation matrix. It should be noted that the transmission matrix can be diagonalized using the eigenvectors $\boldsymbol{u} = \cos(\beta)\,\boldsymbol{x} - \sin(\beta)\boldsymbol{y}$ and $\boldsymbol{v} = \sin(\beta)\,\boldsymbol{x} + \cos(\beta)\boldsymbol{y}$, where $\boldsymbol{x}$ and $\boldsymbol{y}$ are unit vectors. The waveplate orientation, β, and the electrical thickness, $d\Delta n$, are two degrees of freedom that can be adjusted to control T_{Rx} and T_{Lx} at a single frequency to realize a monochromatic linear-to-circular polarizer. The bandwidth can be extended by cascading two waveplates together such that $\boldsymbol{T}_{cas} = \boldsymbol{T}_{wp2}(\beta_2, d_2\Delta n_2)\boldsymbol{T}_{wp1}(\beta_1, d_1\Delta n_1)$. Increasing the number of waveplates increases the degrees of freedom, which allows for designing multi-resonant linear-to-circular polarizers that operate perfectly at multiple frequencies. For example, consider the case where two anisotropic dielectrics are cascaded, as shown in Figure 26(a). The thickness of both layers is 40 mm, which corresponds to $9.3\lambda_h$, where λ_h is the wavelength at the highest operating frequency of 70 GHz. The permittivities of the waveplates are,

$$\varepsilon_1 = \begin{pmatrix} 1.02 & 0.05 & 0 \\ 0.05 & 1.16 & 0 \\ 0 & 0 & 1 \end{pmatrix}, \ \varepsilon_2 = \begin{pmatrix} 1.08 & 0.02 & 0 \\ 0.02 & 1.01 & 0 \\ 0 & 0 & 1 \end{pmatrix} \tag{8}$$

Diagonalizing the permittivities reveals that, $\beta_1, d_1\Delta n_1, \beta_2, d_2\Delta n_2$ equal -17.6°, 3.33 mm, -72.4°, 1.667 mm respectively. As shown in Figure 26(b), the polarizer works perfectly at the two design frequencies of 30 GHz and 60 GHz ($|T_{Rx}| = AR = 0$ dB) and maintains an axial ratio below 3dB below them. The double resonance significantly increases the bandwidth over the case of a single waveplate. Naturally, adding additional waveplates provides more degrees of freedom which can be utilized to enhance bandwidth and/or improve axial ratio throughout the band.

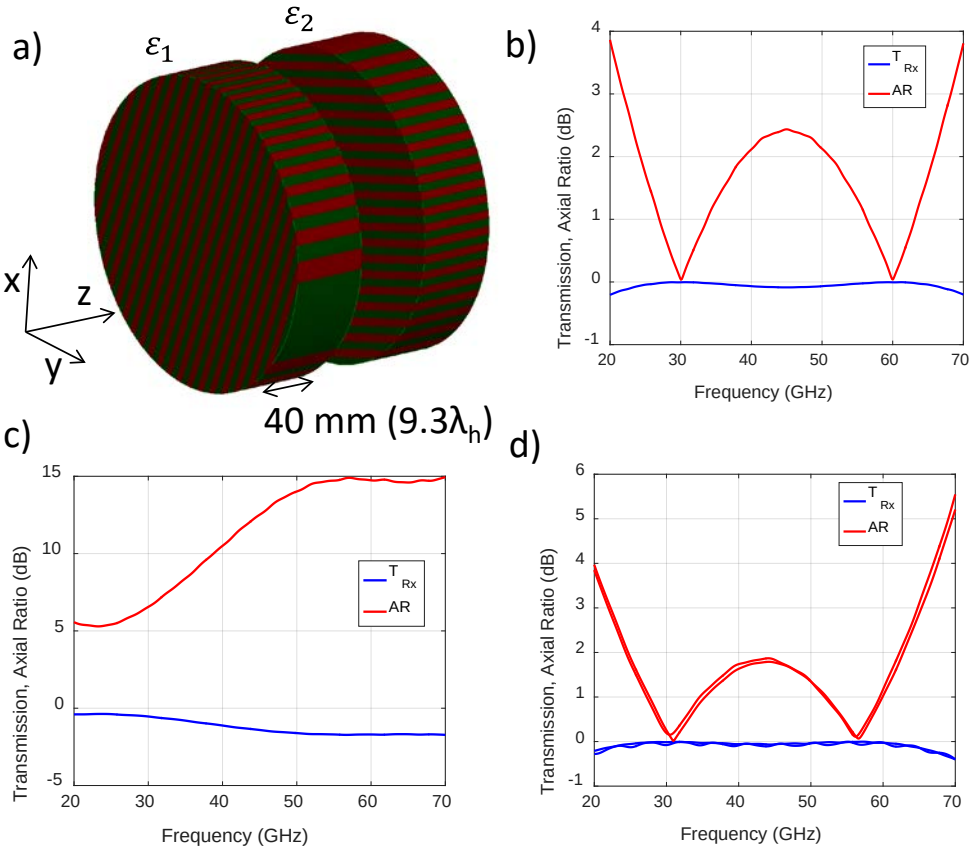

Figure 26: Geometry (a), Performance at Broadside (b), and Performance at 45° *Scan (c) and (d), of Linear-to-Circular Polarizers Consisting of Two Cascaded Waveplates*

An issue with these cascaded waveplate polarizers is the performance is typically sensitive to the angle of incidence. Increasing the angle of incidence increases the amount of time a wave spends within the slab, which in turn increases the effective electrical thickness of each layer. For example, Figure 26(c) plots the response of the same cascaded waveplates when illuminated at 45° from broadside in the E-plane. The performance is significantly degraded compared to normal incidence since the axial ratio is above 5 dB throughout the band.

Two mechanisms are used here to address the sensitivity to oblique angles of incidences. First, the permittivity of the anisotropic material is increased. This bends the wave towards the normal direction as it propagates through the slab in accordance with Snell's law [29]. Therefore, the optical thickness that the wave sees is less dependent upon the angle of incidence. For example, if the angle of incidence is $60°$ and the average permittivity within the waveplates is 3.5, the wave only propagates at $28°$ within the waveplates. However, impedance matching layers need to be added to the front and back of the material which increases complexity and thickness.

Next, the range of incidence angles is increased further by controlling the permittivity in the x, y and z directions. Controlling the permittivity in three principal directions can reduce the index contrast between the two eigenpolarizations at oblique angles, which compensates for the increased optical thickness. For example, if the permittivity in the z-direction is increased such that,

$$\varepsilon_1 = \begin{pmatrix} 1.02 & 0.05 & 0 \\ 0.05 & 1.16 & 0 \\ 0 & 0 & 1.08 \end{pmatrix}, \varepsilon_2 = \begin{pmatrix} 1.08 & 0.02 & 0 \\ 0.02 & 1.01 & 0 \\ 0 & 0 & 1.04 \end{pmatrix} \tag{9}$$

the transmission coefficient and axial ratio at 45^o scan in the E- and H- planes are shown in Figure 26(d). Note that the curves for E- and H- plane scan lie virtually on top of each other. The response at oblique angles is very similar to the broadside case when the z-directed permittivity is properly chosen. It was generally observed that the z-directed permittivity should be near the geometric mean of the u and v directed permittivities (i.e., the transverse permittivities along the principal axes) if the polarizer is expected to work at wide scan angles.

The geometry of the designed cascaded waveplate polarizer is shown in Figure 27. The internal section consists of 4 anisotropic, artificial dielectric slabs with rotated principal axes. The outer section utilizes 3 dielectric matching layers on either side to impedance match the artificial dielectrics to free space. The thickness and orientation of the different layers are optimized using a genetic algorithm implemented in MATLAB. For simplicity the anisotropic dielectric slabs all have the same permittivity. In total there are 14 degrees of freedom that need to be optimized: thickness and permittivity of the 3 matching layers (6 unknowns), and thickness and orientation of the 4 anisotropic dielectrics (8 unknowns).

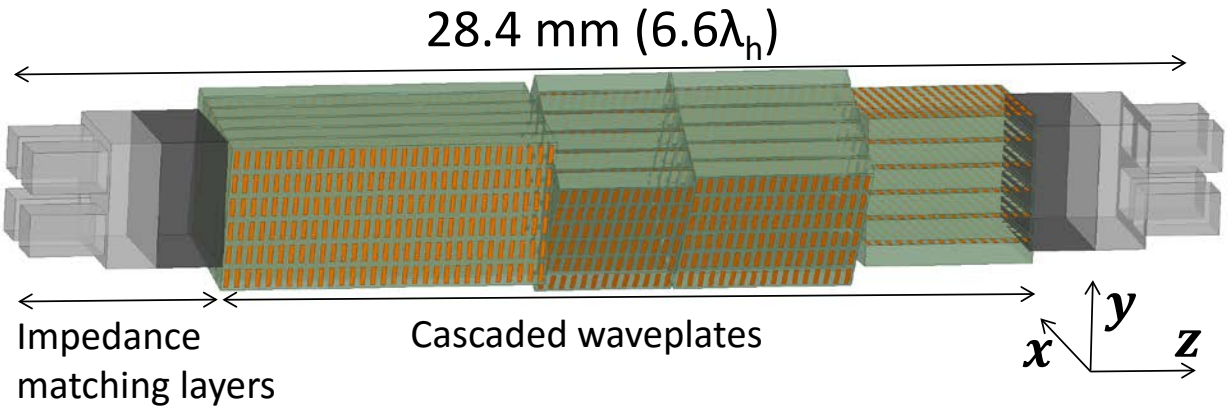

Figure 27: Section of the Designed Linear-to-Circular Polarizer Realized Using Cascaded Waveplates

The genetic algorithm optimization begins with an initial population of 200 randomly seeded individuals. The transmission coefficients, $T_{Rx}(\omega, \theta, \phi)$ and $T_{Lx}(\omega, \theta, \phi)$, of each individual are analytically calculated for normal and oblique angles of incidence using expressions provided in the supplementary material of Ref. [30]. The individuals with lowest cost are selected from the population, randomly mutated, and the process is repeated. The cost function that is minimized is given by,

$$Cost = \sum_{\omega}\left[(1 + |T_{Lx}(\omega, 0°, 0°)| - |T_{Rx}(\omega, 0°, 0°)|)^5 + \sum_{\phi}\left(\frac{(1 + |T_{Lx}(\omega, 60°, \phi)| - |T_{Rx}(\omega, 60°, \phi)|)^5}{10}\right)\right] \quad (10)$$

This cost function maximizes T_{Rx} and minimizes T_{Lx}, which minimizes insertion loss and axial ratio over the desired bandwidth and angles of incidence. The transmission coefficients are calculated at 21 frequency points between 15 GHz and 70 GHz, and at angles of incidence $\theta = 0°, 60°$, and $\phi = -45°, 0°, 45°, 60°$. A larger weight is assigned to the transmission coefficients at normal incidence. The summed elements within the cost function $(1 + |T_{Lx}| - |T_{Rx}|)$ are raised to the 5th power, which helps optimize for the worst case scenario. The optimization process takes on the order of 30 minutes to complete with a 24 core CPU running at 2.5 GHz.

Once the optimal material permittivities and thicknesses are determined, each layer is physically implemented. The impedance matching layers are physically realized by stacking together different substrates. The effective permittivities of the impedance matching layers shown in Figure 27 are 1.3, 1.8, and 2.2, with thicknesses equal to 1.8 mm, 1.2 mm, and 1.6 mm, respectively. A broadband impedance match between free space and the cascaded waveplates is realized by gradually transitioning the permittivity. The permittivity of the outermost dielectric is reduced from 1.8 to 1.3, by milling trenches in the substrate, as shown in Figure 27.

A unit cell of the cascaded, anisotropic waveplates is shown in Figure 28. It is designed using standard dielectric mixing formulas to realize the optimized anisotropic permittivity [31]. The

principal axes of the unit cell are oriented along the u, v, and z directions. Each cell consists of a 0.5 mm thickness Rogers 4003 substrate ($\varepsilon = 3.55$) patterned with a copper patch that is 0.1 mm $\times$ 0.45 mm in size. The copper rectangle primarily increases the permittivity in the v direction, while minimally affecting the permittivity in the u and z directions. The small unit cell size reduces the effects of both temporal and spatial dispersion. The effective permittivity tensor of the unit cell was extracted by illuminating a 10 unit cell thick slab with normally incident plane waves propagating in the z and u directions [32],

$$\begin{pmatrix} \varepsilon_{uu} & \varepsilon_{uv} & \varepsilon_{uz} \\ \varepsilon_{vu} & \varepsilon_{vv} & \varepsilon_{vz} \\ \varepsilon_{zu} & \varepsilon_{zv} & \varepsilon_{zz} \end{pmatrix} = \begin{pmatrix} 2.45 & 0 & 0 \\ 0 & 4.1 & 0 \\ 0 & 0 & 3.2 \end{pmatrix}, \tag{11}$$

The orientation of the different layers are $\beta_1 = 9°$, $\beta_2 = 34°$, $\beta_3 = 29°$, and $\beta_4 = 87°$, for the first through fourth layers, respectively. Their thicknesses are $t_1 = 7.75$ mm, $t_2 = 3.25$ mm, $t_3 = 4.25$ mm, and $t_4 = 4.0$ mm.

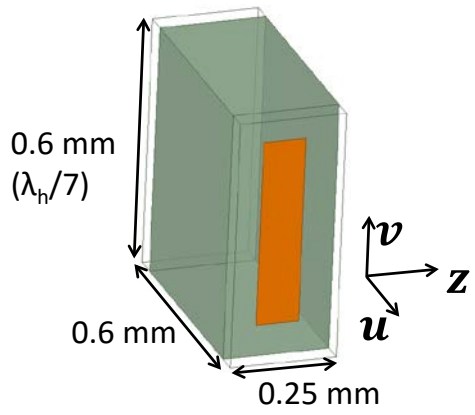

Figure 28: Unit Cell of the Artificial Anisotropic Dielectric

Increasing the anisotropy of the waveplate is beneficial because it reduces the required thickness. In addition, it increases robustness to fabrication tolerances since the performance of a waveplate is proportional to the difference in the indices of refraction along the principal directions (i.e., $\sqrt{\varepsilon_{vv}} - \sqrt{\varepsilon_{uu}}$). To illustrate this point, consider a single waveplate illuminated at normal incidence with $\varepsilon_{uu} = 3.2$ and $\varepsilon_{vv} = 3.5$ that converts an incident linear polarization to circular polarization. If the permittivity of $\varepsilon_{vv} = 3.5$ is reduced by 5% due to fabrication tolerances, the axial ratio of the transmitted field will increase from 0 dB to 7.5 dB. However, if the designed permittivity contrast is increased such that $\varepsilon_{uu} = 2$ and $\varepsilon_{vv} = 3.5$, a 5% decrease in ε_{vv} only increases the axial ratio to 1 dB. On the other hand, the permittivity contrast should not be increased too much since this makes it more difficult to impedance match the waveplates to free space using isotropic dielectrics.

It should be noted that the cascaded waveplates cannot be simulated as a single unit cell in a periodic lattice since the principal axes of each anisotropic layer are all different. Therefore, the simulated S-parameters of the polarizer are calculated by simply cascading the S-parameters of the individual waveplates. This technique assumes the field at the boundary between two

different waveplates is accurately represented by the fundamental Floquet modes, which are propagating plane waves with TE and TM polarizations. In other words, the simulation neglects evanescent coupling between the different waveplates, which is expected to contribute only minor influences to the polarizer's response. Note that the circuit solver in HFSS provides a convenient method of cascading the S-parameters of the individual waveplates.

The simulated transmission coefficient and axial ratio when illuminated with an x-polarized plane wave is shown in Figure 29 for different angles of incidence. At normal incidence, the transmission coefficient (T_{Rx}) is above -1 dB between 11 GHz and 72 GHz, and the axial ratio (AR) is below 3 dB from 15 GHz to 70 GHz (4.7:1 bandwidth). The polarizer also performs well at oblique incidence as shown in Figure 29 (b) and (c). When illuminated at $60°$ from normal incidence in the E, H, and diagonal planes, the peak axial ratio increases to 4 dB within the operating band of 15 GHz to 70 GHz. A 4 dB axial ratio corresponds to a cross-polarization level of -12.9 dB, which is satisfactory for many systems. It should be noted that while the polarizer is only designed to work for x-polarized incident waves, the symmetry of the geometry provides a similar performance when the incident wave is y-polarized. However, a y-polarized wave would be converted to left-handed circular polarization.

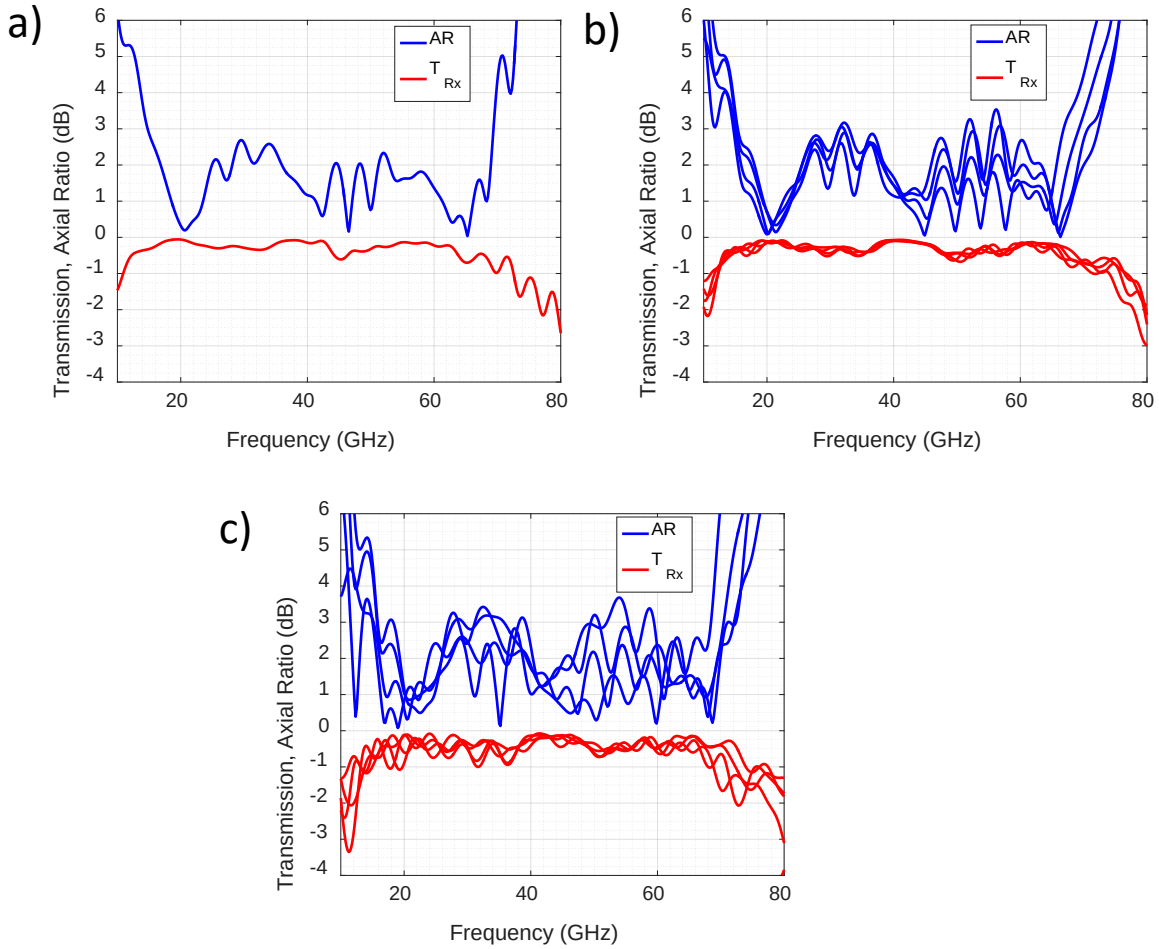

Figure 29: Simulated Performance of the Cascaded Waveplate Polarizer at Normal Incidence (a), 45° scan (b), and 60° scan (c) in the E, H, and D planes

5.4.2 Cascaded Sheet Impedance Polarizer

The next approach to realizing an ultrawideband polarizer is inspired by the microwave engineering community. Meanderline polarizers utilizing cascaded sheets of meandered wires were first introduced in [25]. These polarizers effectively reduce the permittivity along the direction of the wire, and increase the permittivity in the orthogonal direction, which provides an anisotropic response to control the polarization [26]. Previous polarizers typically aligned the principal axes of all layers in the $\boldsymbol{x} + \boldsymbol{y}$ and $\boldsymbol{x} - \boldsymbol{y}$ directions (i.e., $\beta = 45°$), similar to the case of linear-to-circular polarizers constructed from single waveplates. Bandwidths of up to 2:1 have been realized with meanderline polarizers by engineering the frequency dispersion along their two principal axes [29]. However, as the bandwidth is increased, the performance at wide scan angles tends to suffer [27].

In this subsection, an ultrawideband linear-to-circular polarizer is realized by modifying the conventional geometry of a meanderline polarizer. It was shown in the previous subsection that

rotating the principal axes of the various layers increases the useful design degrees of freedom, which can be leveraged to enhance bandwidth. Therefore, the orientation (i.e., rotation) of each sheet is a free variable that is optimized. Furthermore, each sheet is not restricted to only meanderline geometries, which provides additional degrees of freedom. In other words, the layers are best represented as general, anisotropic sheet impedances. Furthermore, higher permittivity substrates are utilized to improve the performance at wide angles of incidence. As mentioned earlier, higher permittivity substrates force the incident wave to bend towards the normal direction, thus reducing the variation with angle of incidence [29].

A section of the cascaded sheet impedance polarizer is shown in Figure 30. The sheets are expanded in the z-direction by a factor of 3 for clarity in Figure 30 (a), while a to-scale version is shown in Figure 30 (b). Again, a genetic algorithm optimization in MATLAB is used to design the polarizer. The polarizer consists of impedance matching layers on the outside, and cascaded anisotropic metallic patterns printed on Rogers 4003 substrates in the middle. The permittivity of the 4003 substrate ($\varepsilon = 3.55$) is large enough to improve the performance at wide scan angles, but not too large such that it is not difficult to provide a broadband impedance match to free space. In total, 8 patterned copper sheets are used, which are spaced 0.4 mm apart in the z-direction. This results in roughly 25 unknowns that need to be optimized: thickness and permittivity of the 3 matching layers (6 unknowns), and dimensions (roughly 11 unknowns) and orientation (8 unknowns) of the patterned metallic sheets. Again, the cost function given by (10) is used, which minimizes insertion loss and axial ratio over the operational bandwidth at normal and oblique angles of incidence.

Two different metallic geometries are considered for each sheet: meanderline and metallic patches, as shown in Figure 30 (c) and (d). Parametric sweeps were performed using ANSYS HFSS to extract the anisotropic sheet impedances of the patterned metallic geometries as a function of their dimensions (L_m, P_u, and L_p) and frequency, at normal incidence. Simulations demonstrated that the sheet impedance is not a strong function of the angle of incidence. Interpolation is used to approximate the sheet impedance of geometries that are not explicitly simulated. The dimension L_m primarily controls the inductance of the meanderline in the v-direction, while P_u determines the capacitance in the u-direction. The dimension L_p primarily affects the capacitance of the patch along the v-direction. The simulated sheet impedances are inserted into a MATLAB routine that analytically calculates the S-parameters of the cascaded structure [33]. This routine is used by the genetic algorithm to optimize the dimensions and orientation of each sheet.

A brute force sweep is used to determine which sheets utilize meanderline geometries and which sheets utilize patches. First, every sheet is forced to be of the metallic patch geometry, and the genetic algorithm finds the minimum cost for this case by optimizing L_p, and β of each sheet, as well as the permittivity and thickness of the impedance matching layers. Then, the first sheet is replaced with the meanderline geometry and again the minimum cost is calculated using the geometric algorithm. This process is repeated until every possible combination of meanderline and patch geometry is considered, of which there are a total of $2^8 = 256$ combinations. At the end, the meanderline/patch combination with the lowest calculated cost is chosen. The optimal combination utilizes meanderline geometries on the first, third, and seventh sheets. However, it

should be noted that many other options provided a similar performance. The entire optimization process required on the order of few days to complete with a 24 core CPU running at 2.5 GHz.

The optimized dimensions of each patterned metallic sheet are shown in

Table 1. The effective permittivities of the impedance matching layers shown in Figure 30(a) are 1.3, 1.8, and 3.0, with thicknesses equal to 1.8 mm, 1.2 mm, and 0.75 mm, respectively.

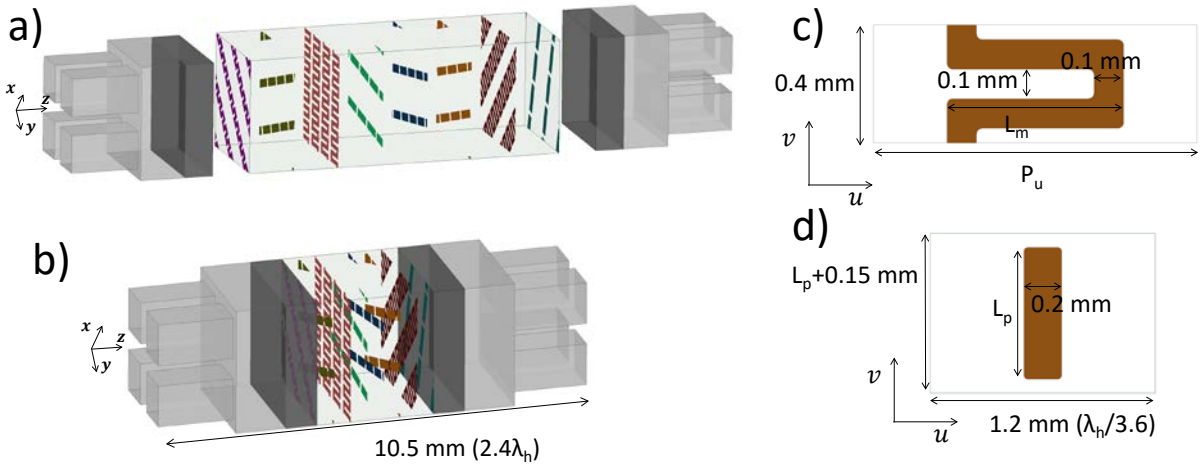

Figure 30: Section of the Cascaded Sheet Impedance Polarizer (a) and (b), and Dimensions of the Meanderline (c) and Patch (d) Geometries Comprising the Different Sheets

Table 1: Dimensions and Orientation of the 8 Different Sheets Comprising the Cascaded Sheet Impedance Polarizer

Sheet#	L_m (mm)	P_u (mm)	L_p (mm)	β (deg.)
1	0.28	0.98	NA	5
2	NA	NA	0.63	118
3	0.60	0.84	NA	46
4	NA	NA	0.70	143
5	NA	NA	0.55	126
6	NA	NA	0.78	119
7	0.60	1.10	NA	89
8	NA	NA	0.76	60

Again, it was not possible to rigorously simulate the entire polarizer using a full-wave solver. Instead, the S-parameters of the different layers are cascaded together using the circuit solver in HFSS to calculate the S-parameters of the overall structure. Full wave simulations of similar geometries that are periodic verified that simply cascading S-parameters provides an accurate estimate of the overall performance. In other words, evanescent coupling between the different layers can be neglected for these cells sizes and interlayer spacing. The simulated performance is shown in Figure 31. At normal incidence, the transmission coefficient (T_{Rx}) is above -1 dB between 15 GHz and 72 GHz, and the axial ratio is below 3 dB from 16 GHz to 68 GHz (4.2:1 bandwidth). Again, the polarizer performs well at oblique incidence. When illuminated at $60°$ from normal incidence in the E, H, and diagonal planes, the peak axial ratio increases to 4 dB within the operating band. It should be noted that this polarizer does not efficiently convert incident y-polarized waves into circular polarization, in contrast to the vast majority of previously published linear-to-circular polarizers. This is because the first sheet has a low inductance in the y-direction, which acts as a wire-grid polarizer that reflects y-polarized waves.

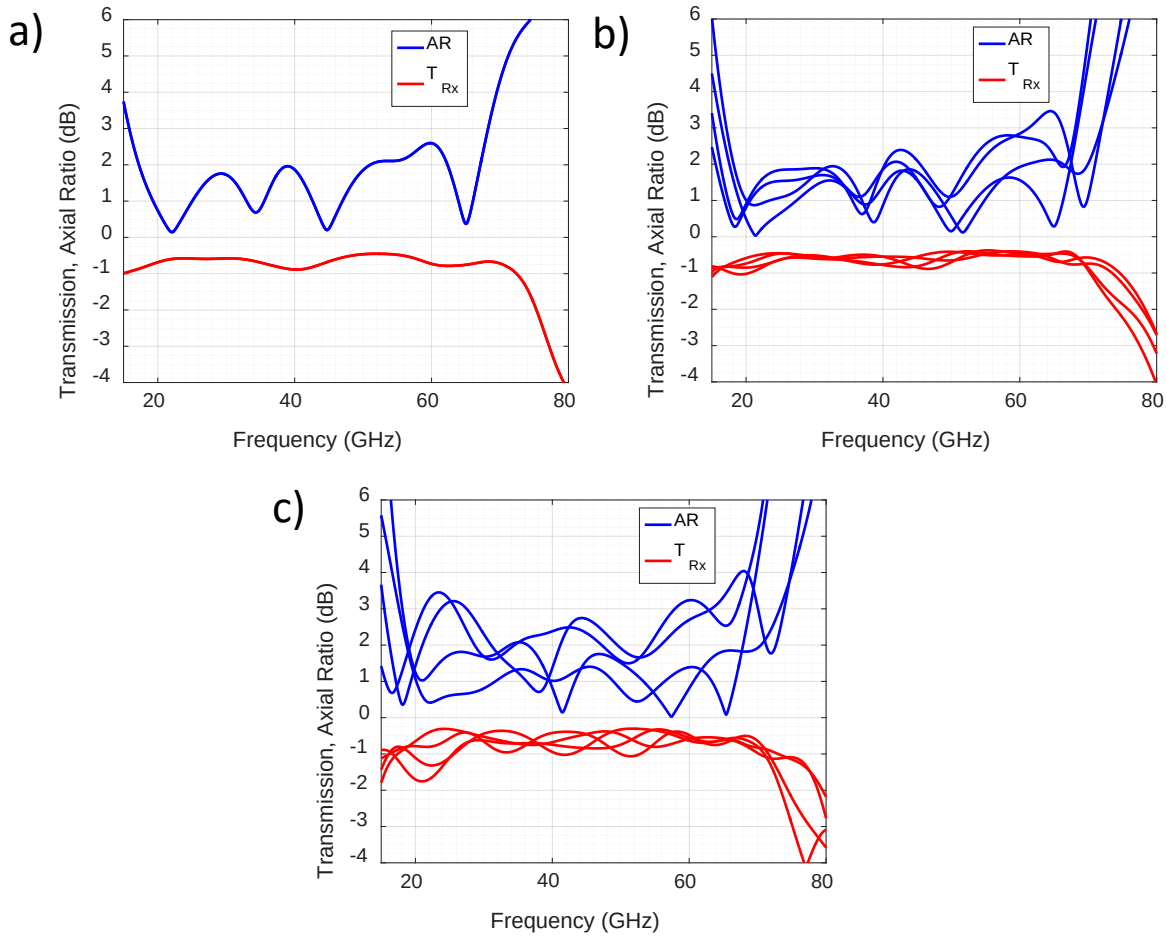

Figure 31: Simulated Performance of the Cascaded Sheet Impedance Polarizer at Normal Incidence (a), 45° scan (b), and 60° scan (c) in the E, H, and D planes

5.5 Measurements

5.5.1 Experimental Setup

Both linear-to-circular polarizers were fabricated and measured using the Gaussian beam telescope shown in Figure 32 [34]. This system generates an incident Gaussian beam with beam waist diameter roughly equal to 3λ, which significantly reduces the required fabricated area compared to the case where a single lens or no lenses are used. The system operates between 15 GHz and 110 GHz. The Gaussian beam telescope consists of 2 linearly polarized standard gain horn antennas on either side of the polarizer under test. The horns have a high gain (~23 dB), and their radiated beams are quasi-Gaussian (85% coupling to the fundamental Gaussian mode). In order to characterize the polarizers across the wide operating bandwidth, four different standard gain horn antennas were used to cover the K, Ka, V, and W bands. The horns are connected to a 2-port network analyzer that is integrated with frequency extenders to allow for measurements of the S-parameters up to 110 GHz. The system utilizes 4 plano-convex Teflon lenses with 100 mm diameters and 150 mm focal lengths. The lenses are separated from each other by the sum of

their focal lengths (300 mm), which generates a collimated quasi-Gaussian beam at the center of the system with unity magnification at all operating frequencies [34]. The polarizers are mounted on a 3D printed rotation stage that allows for measuring the transmission coefficients at normal and oblique incidence, along different planes (e.g., E, H, and diagonal planes). The beam waist diameter at the lower operating frequencies (15 GHz) is calculated to be ~50 mm, and it reduces as the frequency increases. Therefore, the cross sectional diameter of the polarizer needs to be at least 50 mm. Note that orienting the polarizer for measurements at oblique angles reduces the effective cross sectional area seen by the incident Gaussian beam. For example, a 60° scan angle effectively reduces the fabricated polarizer's area by half.

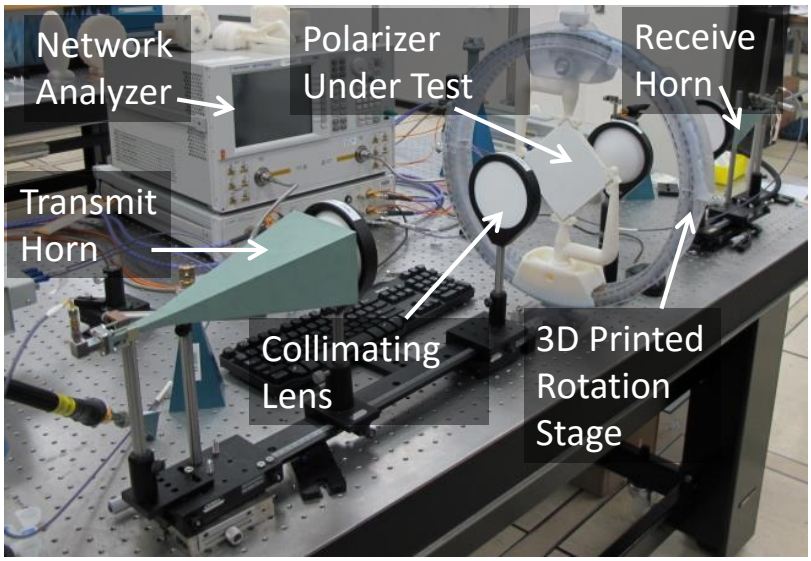

Figure 32: Gaussian Beam Telescope Used to Characterize the Fabricated Polarizers

Linearly-polarized horn antennas are used to measure the polarizers. However, characterizing the linear-to-circular transmission matrix requires knowledge of the transmitted field along two independent polarizations. Conceptually, the simplest method of characterizing the transmitted field is to first orient the receive horn to receive x-polarization, and then rotate the horn by 90° to receive y-polarization. Once T_{xx} and T_{yx} are known, it is straightforward to calculate T_{Rx}, T_{Lx}, or equivalently the insertion loss and axial ratio. However, this approach can be inaccurate since the phase center of the receive horn can easily shift when it is physically rotated. Therefore an alternative approach is taken here. First, the two horns are oriented to measure T_{xx}. To measure an additional component of the transmitted polarization, a wire-grid polarizer oriented along the $\boldsymbol{x + y}$ direction is inserted into the path of the Gaussian beam, after the polarizer under test. The transmission coefficients of the wire-grid polarizer along its two principal axes are independently measured so that its presence can be properly calibrated. By utilizing measurements with and without the wire-grid polarizer in the beam's path, it is possible to extract the transmitted field along two independent polarizations. These measurements are used to characterize the two most relevant characteristics of the fabricated polarizers: T_{Rx} and transmitted axial ratio.

5.5.2 Cascaded-Waveplate Polarizer

The cascaded waveplate polarizer is fabricated by stacking together chemically etched printed-circuit-boards, as shown in Figure 33. One of the fabricated PCBs for the first waveplate is shown in Figure 33(a). This PCB is stacked together with 83 identical PCB's in the u-direction (see Figure 28) to realize the first waveplate. The designed 0.1 mm air gap between the stacked PCBs (in the u-direction) is realized by placing 0.1 mm shims between the boards at their edges. The same process is used to realize the other three waveplates as well. The 4 different cascaded waveplates are shown in Figure 33(b). They are spread apart in the figure for clarity. The fully assembled cascaded waveplate polarizer is shown in Figure 33(c). 3D printed holders support each PCB in the proper orientation. Due to limited time and resources, the fabricated diameter of the cascaded waveplate polarizer is only 50 mm. This diameter is roughly equal to the incident Gaussian beam size at the lower operating frequencies. Therefore, the polarizer is not large enough to be characterized at oblique angles of incidence. The overall size of the polarizer including the 3D printed PCB holders is 120 mm x 120 mm x 28.4 mm.

The cascaded waveplate polarizer's measured (solid curve) and simulated (dashed curve) transmission coefficient (T_{Rx}), and axial ratio (AR) at normal incidence are shown in Figure 34. There is good agreement between measurement and simulation. The gap in measured frequencies at 67 GHz corresponds to the location where the network analyzer switches modes between using internal signal generators (below 67 GHz) and external frequency extenders (above 67 GHz). The measured axial ratio is below 3 dB between 19 GHz and 76 GHz (4:1 bandwidth), and the insertion loss is below 2.5 dB over this frequency range. The insertion loss of the measurements is about 0.5 dB larger than simulations, which could be due to fabrication tolerances, metal surface roughness, and/or air gaps between the 4 different waveplate sections and impedance matching layers.

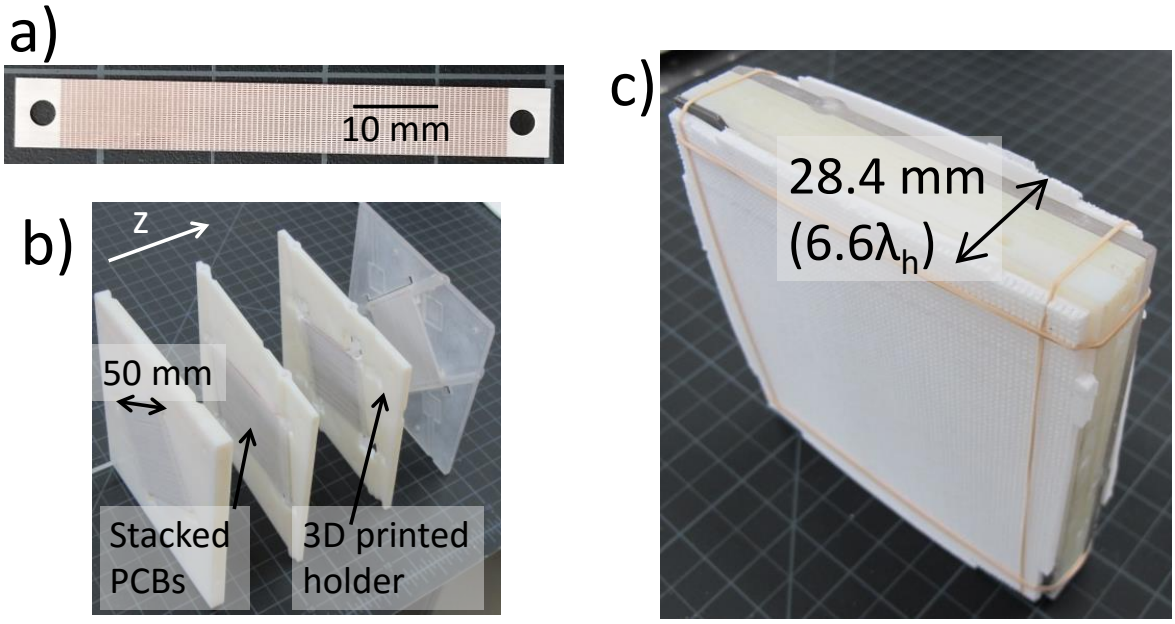

Figure 33: Fabricated Cascaded Waveplate Polarizer

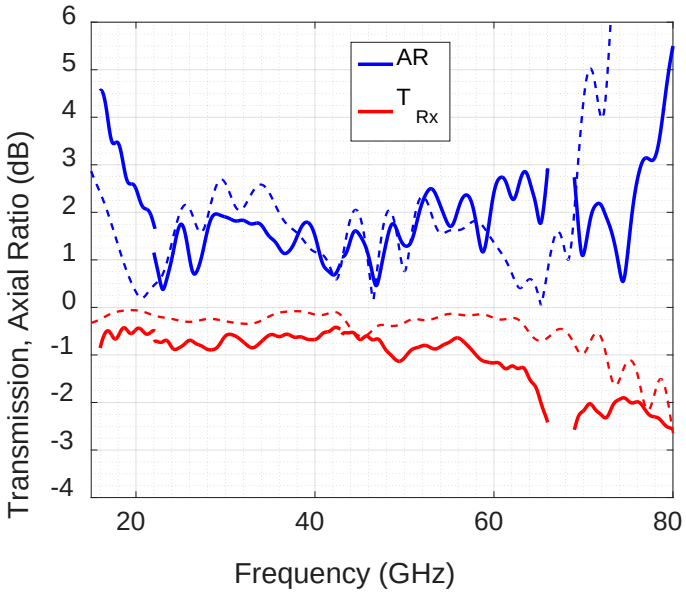

Figure 34: Simulated and Measured Performance of the Cascaded Waveplate Polarizer at Normal Incidence

5.5.3 Cascaded Sheet Impedance Polarizer

The cascaded sheet impedance polarizer is fabricated using standard PCB processing techniques. Each sheet is chemically etched and then bonded together. The fabricated sheets before bonding are shown in Figure 35(a). The finished polarizer after bonding and securing the impedance matching layers is shown in Figure 35(b). The dimensions of the meanderline polarizer are 120 mm x 120 mm x 10.5 mm.

The measured and simulated performance of the cascaded sheet impedance polarizer is shown in Figure 36(a) for normal incidence in the solid and dashed curves, respectively. The measured insertion loss is below 1.5 dB between 16 GHz and 73 GHz, and the axial ratio is below 4.5 dB over this frequency range. There is reasonable agreement between simulation and measurement. The larger measured axial ratio at 60 GHz is attributed to fabrication tolerances. The cascaded sheet impedance polarizer was also characterized at oblique angles of incidence ($\theta = 45°,\ 60°$), along the E, H, and diagonal planes ($\phi = 0°, 45°, 90°, 135°, 180°, 225°, 270°, 315°$ planes). The performance only slightly degrades as the angle of incidence is increased to 45° from normal, as shown in Figure 36 (b). At 60° from normal, the average insertion loss and axial ratio increases by roughly 1 dB compared to the broadside case. Therefore, the performance of the polarizer is quite robust to illumination at different angles of incidence.

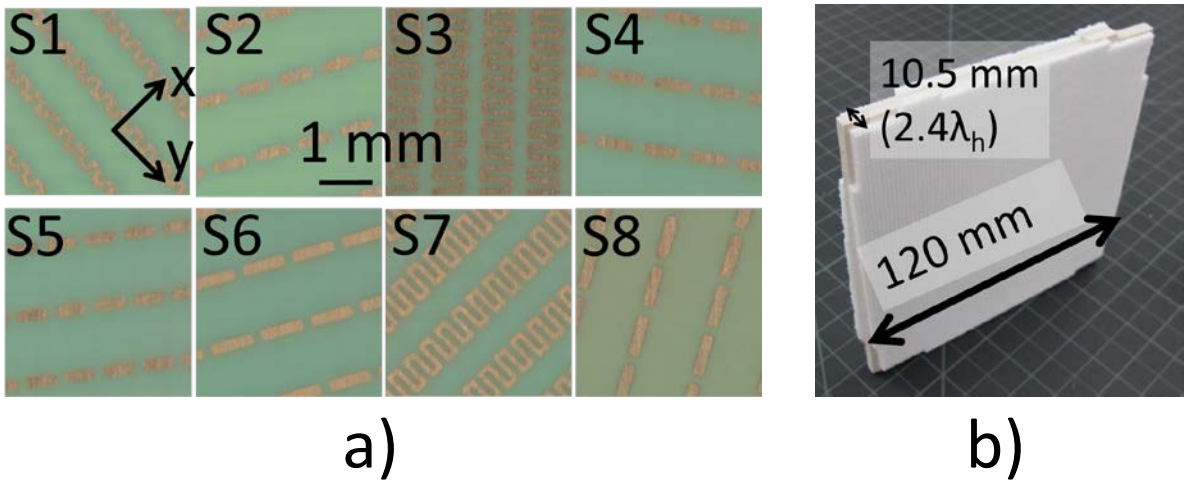

Figure 35: Fabricated Cascaded Sheet Impedance Polarizer

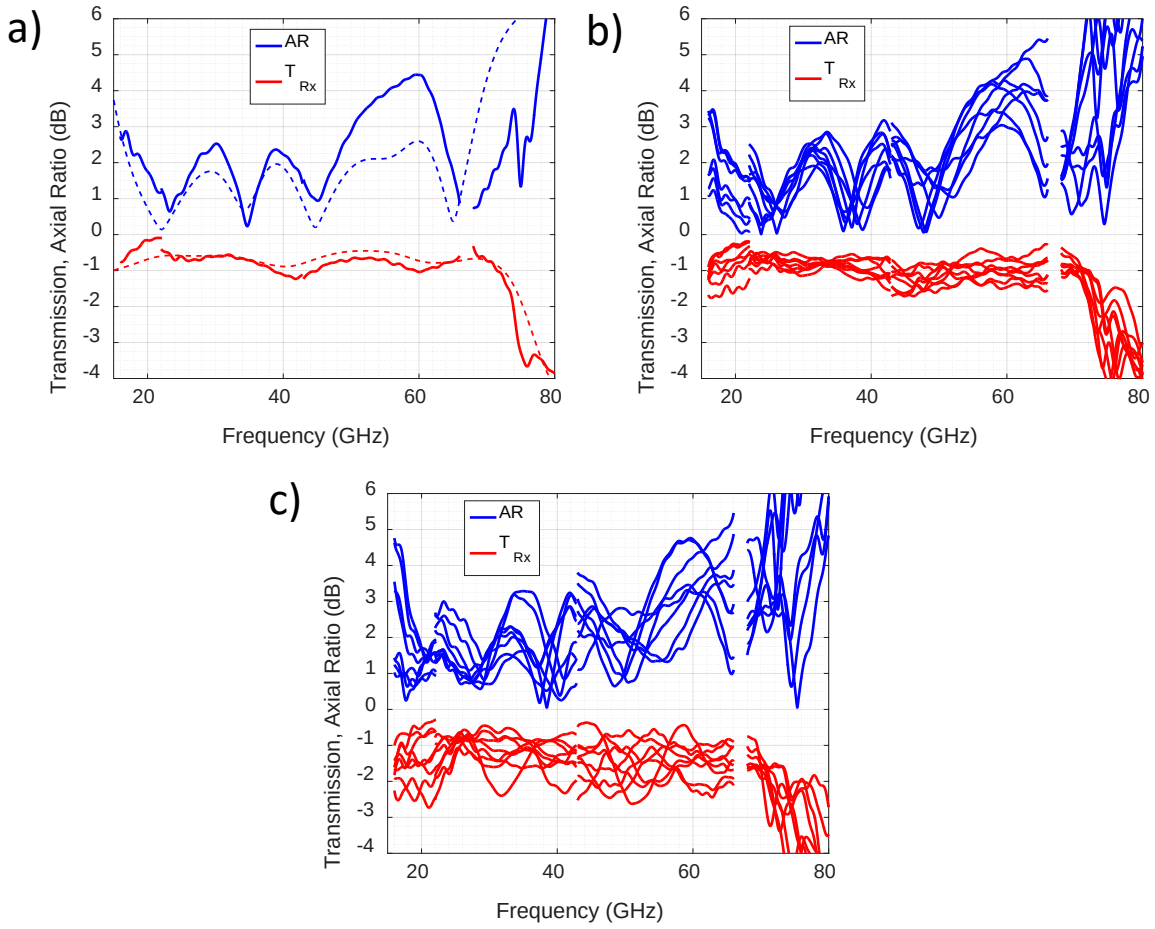

Figure 36: Measured Performance of the Cascaded Sheet Impedance Polarizer at Normal Incidence (a), 45° scan (b), and 60° scan (c) in the E, H, and D planes

5.5.4 Refined Cascaded Sheet Impedance Polarizer

For many applications, an axial ratio below 3 dB is desired. Unfortunately, fabrication tolerances increased the axial ratio of the cascaded sheet impedance prototype to 4.5 dB near 60 GHz. The performance could likely be improved by exploiting statistical variations in the fabrication process. Many polarizers could be fabricating and measured, and the polarizers with best performance could be picked out. However, this process would be expensive and time consuming for demonstrating a proof-of-concept.

Instead, the fabricated polarizer is refined by adding an additional anisotropic layer to compensate for the higher axial ratio near 60 GHz. The 3D printed dielectric grating made from VeroWhite ($\varepsilon = 2.8$), shown in Figure 37, is embedded within the impedance matching layers (sandwiched between the $\varepsilon = 3$ and $\varepsilon = 1.8$ layers). A side view of the designed grating is shown in the inset. The grating generates a simulated relative phase shift difference of 7° between the u and v polarizations at 60 GHz, which in turn brings the transmitted phase shift

difference between x and y polarizations closer to the ideal 90° at the higher operating frequencies. The phase shift difference between u and v polarizations is directly proportional to the frequency. Therefore, the additional grating negligibly affects the performance at the lower operating frequencies. The measured performance at normal incidence and 60° scan angles is shown in Figure 38. The presence of the dielectric grating keeps the axial ratio below 3 dB from 17 GHz to 66 GHz at normal incidence. Again, the polarizer's performance only marginally degrades when illuminated at wide scan angles. However, it should be noted that the dielectric grating does increase the insertion loss at some frequencies and angles of incidence. This process of fabricating an additional 3D printed dielectric layer to refine the performance of polarization controlling devices is extremely simple and inexpensive.

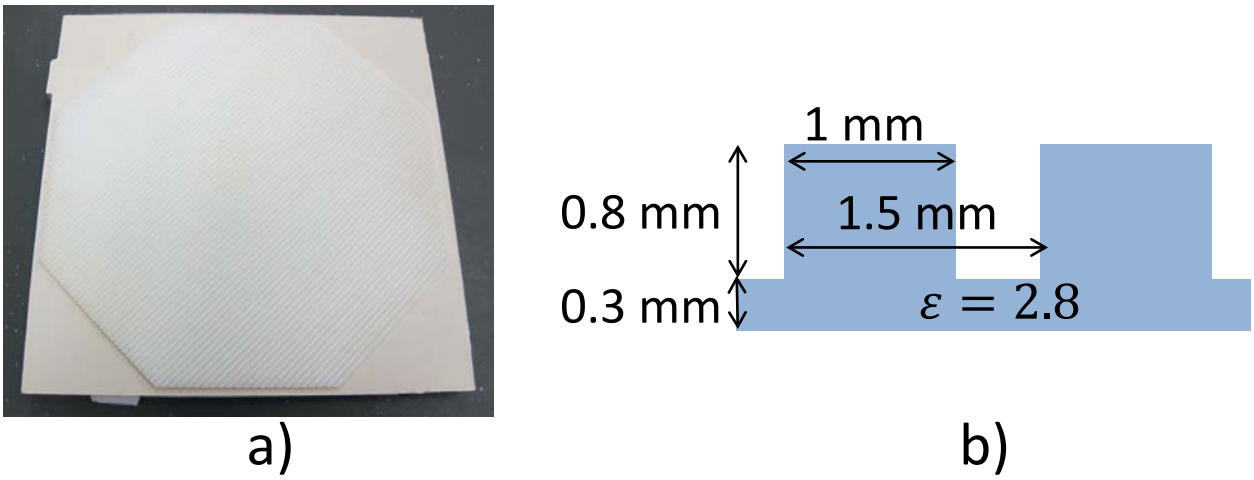

Figure 37: Fabricated Dielectric Grating Used to Refine the Performance of the Cascaded Sheet Impedance Polarizer (a), and a Side-View Schematic of the Designed Grating.

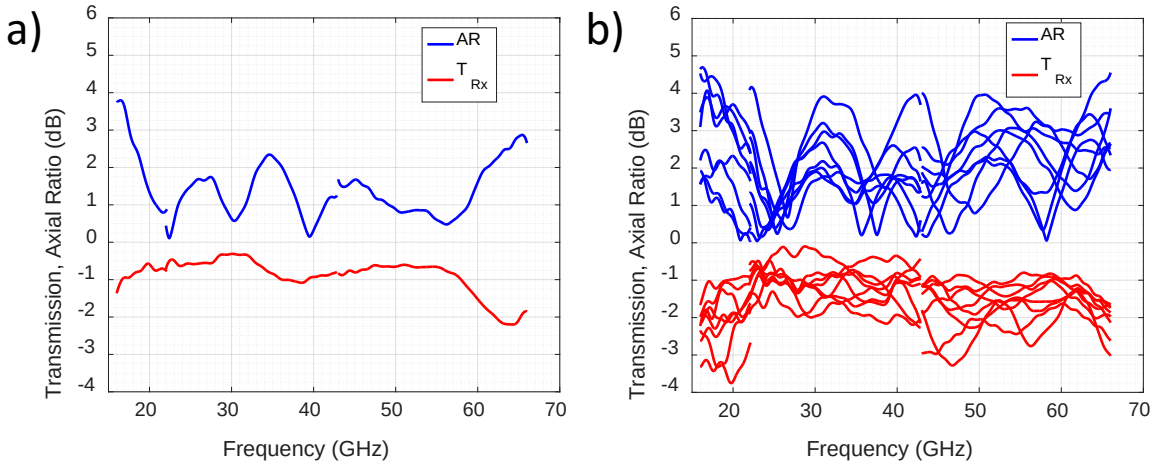

Figure 38: Performance of the Cascaded Sheet Impedance Polarizer With the Integrated Dielectric Grating Measured at Normal Incidence (a) and 60° Scan in the E, H, and D-planes

5.6 Summary

Ultra-wideband linear-to-circular polarizers that work at wide scan angles are presented at mm-wave frequencies. The polarizers are on the order of a few wavelengths in thickness to maintain a 3 dB axial ratio and 1 dB insertion loss over a 4:1 bandwidth. Both polarizers rely on a genetic algorithm to optimize roughly 20 design variables. The optimizations converge reasonably fast (on the order of hours) since a combination of analytic modeling and full wave simulation is used rather than purely full wave simulations. It should be emphasized that the design methodologies reported here are by no means unique. The most important aspect of the design process is to use a global optimization algorithm (e.g., genetic algorithm) to optimize many independent degrees of freedom for minimizing the specified cost function.

The cascaded waveplate polarizer is particularly simple to design since it is accurately modeled using effective material parameters whose response can be calculated analytically. The bandwidth of this polarizer could be increased further by simply adding more layers. However, it requires a nonstandard fabrication process and is many wavelengths in thickness, which can be undesirable for some applications. The cascaded sheet impedance polarizer is significantly thinner and easier to fabricate than the cascaded waveplate polarizer. However, the cascaded sheet impedance polarizer is more difficult to design since full wave simulations need to be integrated into the optimization process.

It is likely that the performance of both devices can be improved further by increasing the degrees of freedom. In particular, additional layers could be added at the expense of increased thickness. The cascaded waveplate polarizer could also benefit from considering additional metallic geometries other than patches and meanderlines. A particularly nice feature of design by optimization is that modifying the cost function makes it straightforward to tradeoff between relevant design parameters such as maximum scan angle, bandwidth, size, and weight. Thus, the techniques reported here are very general, and could be used to design polarization transforming devices for a variety of applications [33].

6.0 Combining the Antenna and polarizer

6.1 Introduction

Simulations and measurements showed that the linearly polarized antenna array and the cascaded sheet impedance polarizer both work independently of each other. The next task is to assess how well the two components work when they are integrated together. In this section, it is shown through simulations that the expected antenna effiecicny of the circularly polarized array is 60%, and the axial ratio is below 4 dB when scanned up to $60°$ from broadside. In addition, the required area of the linear-to-circular polarizer is estimated using 2D simulations and ray tracing arguments. A 1:256 corporate feed network is also designed with an insertion loss that varies between 5 dB and 15 dB as the frequency is scanned from 20 GHz to 60 GHz. Finally, the feed network, Vivaldi array, and linear-to-circular polarizer are combined to provide a full picture of the system.

6.2 Antenna with Superstrate

A unit cell of the linearly polarized antenna is shown in Figure 39. The element is a short Vivaldi antenna ($\lambda/2.5$ long at the highest operating frequency). The short length improves the polarization purity when the antenna is scanned along the diagonal plane. In addition, an orthogonal metallic wall is placed at the top and bottom of the unit cell which improves the polarization purity further since the radiated wave sees a quasi-parallel-plate environment. The metallic wall is loaded with resistors to dissipate any energy that is reflected from the linear-to-circular polarizer into the orthogonal polarization (y-polarization). If the resistors are removed (or short circuited), reflections from the linear-to-circular polarizer degrade the polarization purity and generate undesired resonances when it is placed on top of the antenna. The antenna is not optimized to radiate into free space since a polarizer will be placed on top of it anyway. Instead, the antenna is designed to be impedance matched to a Rogers Duroid ($\varepsilon = 2.2$) superstrate. It should be noted that it is easier to impedance match the antenna to a lower impedance material (i.e., permittivity greater than unity) since its impedance is closer to the $50\ \Omega$ port impedance of the input transmission line. However, placing a lower impedance material on top of the antenna does reduce the maximal operating frequency since surface waves can be excited at a lower frequency.

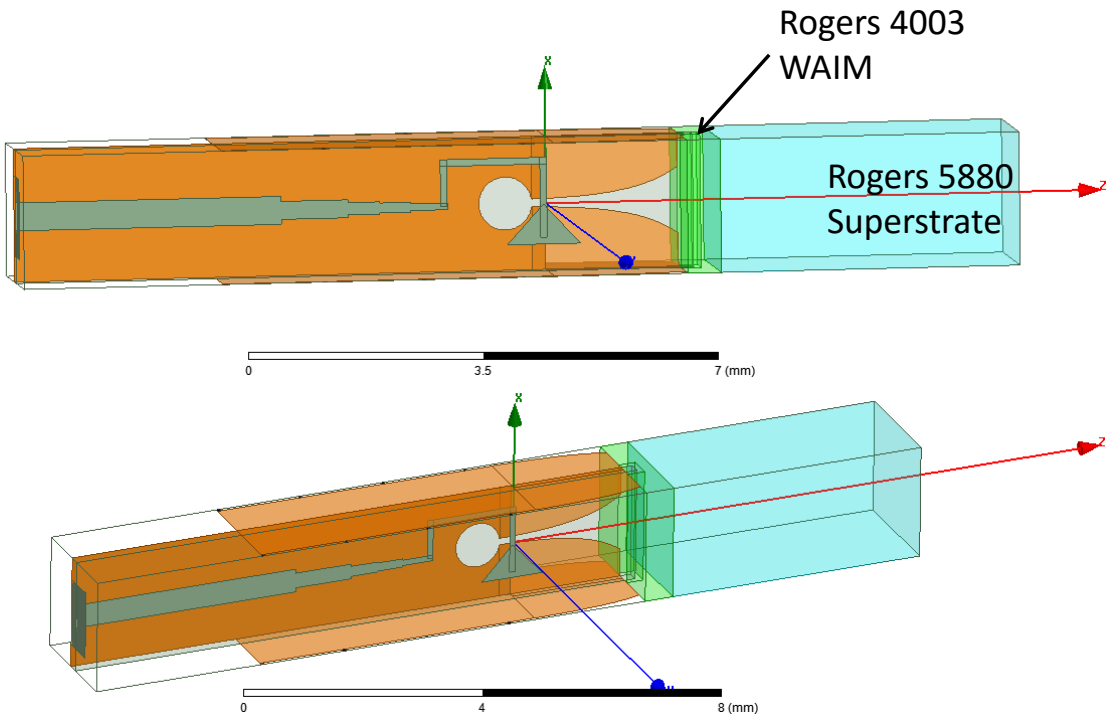

Figure 39: Two different Perspectives of the Linearly-Polarized Vivaldi Array that Radiates into a Rogers 5880 superstrate

The performance of the linearly-polarized antenna without the polarizer on top is shown in Figure 40. The antenna is well matched from 16 GHz to 62 GHz. The cross polarization is also quite low across the band when scanned up to 60° from broadside. The performance at wide scan angles is significantly improved by the presence of the Duroid superstrate. The superstrate refracts the wave towards the normal direction such that scanning the beam to 60° in free space is equivalent to scanning the beam to 36° in the superstrate.

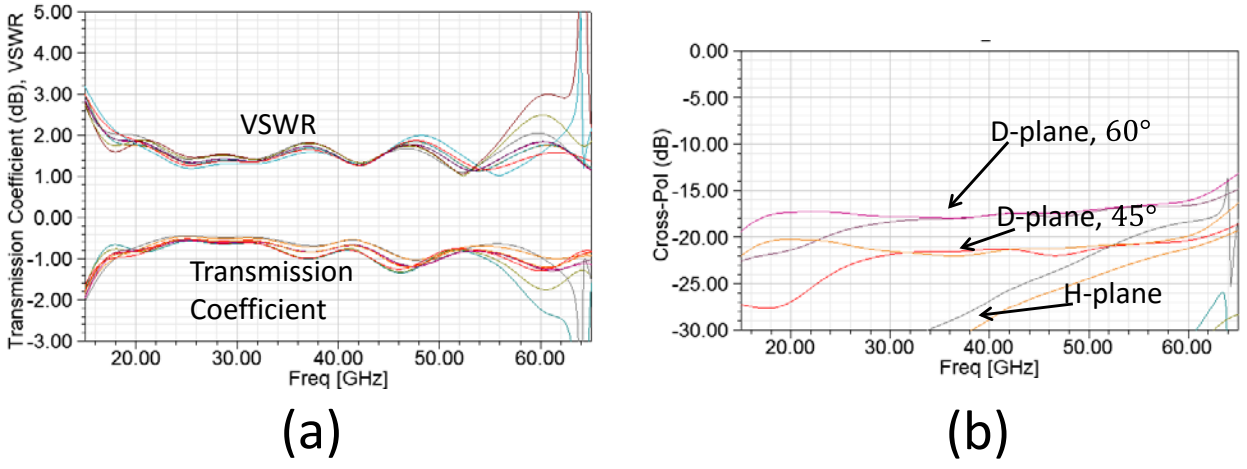

Figure 40: Performance of the Infinite Vivaldi Array

6.3 Antenna-Polarizer Combination

Next, the cascaded sheet impedance polarizer is placed on top of the antenna and the performance of the cascaded structure is characterized. The first two impedance matching layers on the front of the polarizer are removed, since it should to be impedance matched to the Duroid superstrate ($\varepsilon = 2.2$), rather than free space. The geometry of the simulated structure is shown in Figure 41. In Figure 41(b), the cascaded metallic sheets are expanded by a factor of 3 in the z-direction for clarity. Again, it is not possible to rigorously simulate the cascaded unit cell geometry using a full wave solver since the different metallic layers of the linear-to-circular polarizer have different periodicities and orientations. Instead, the S-parameters of each component are cascaded together using the circuit solver in HFSS. The circuit diagram with the cascaded components is shown in Figure 42.

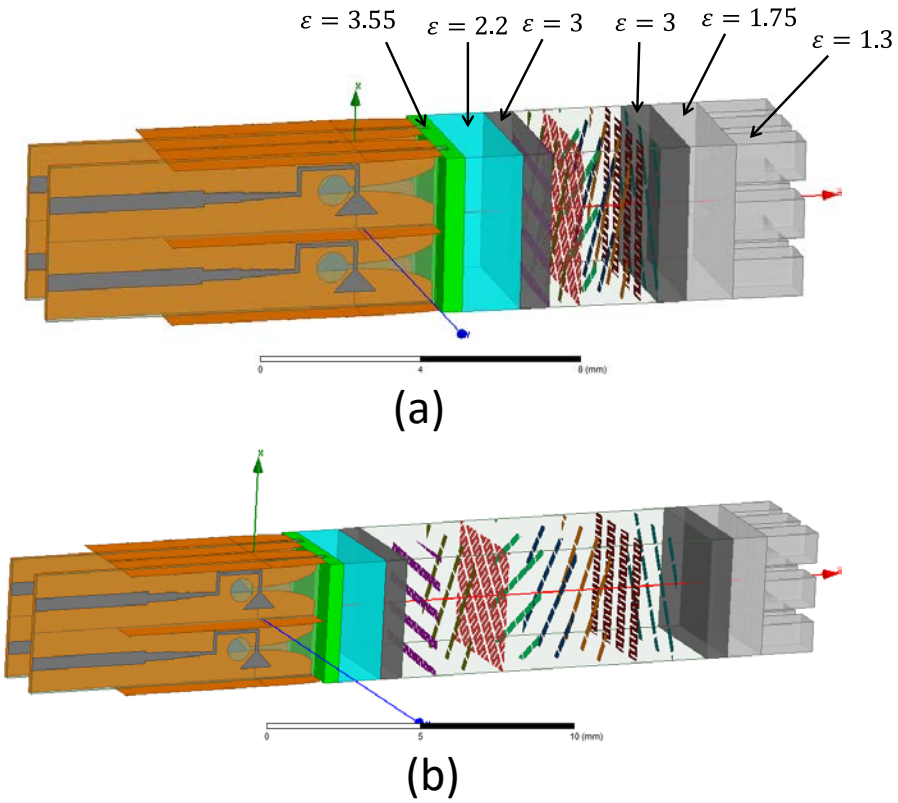

Figure 41: Linearly Polarized Vivaldi Array Combined with the Cascaded Sheet Impedance Polarizer

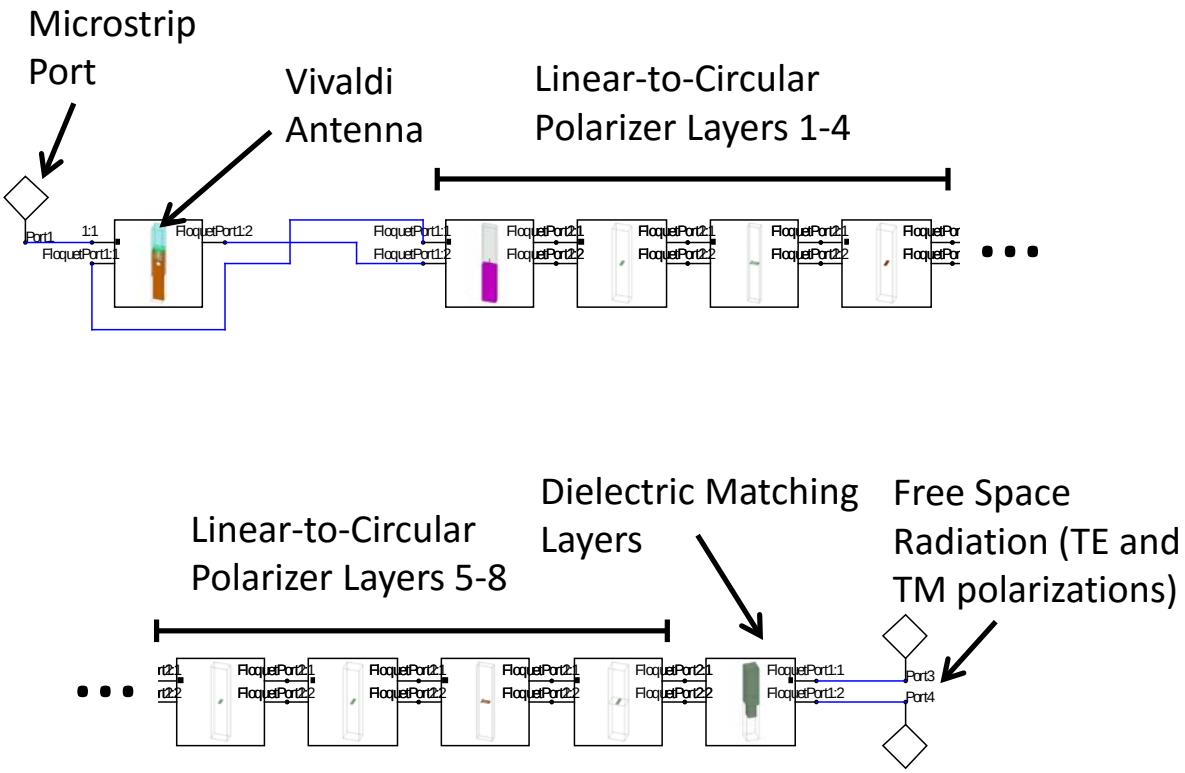

Figure 42: Circuit Model Used to Cascaded the S-parameters of the Vivaldi Antenna and Linear-to-Circular Polarizer.

The simulated performance is shown in Figure 43. At broadside, the transmission coefficient is greater than -2 dB and axial ratio is below 3 dB at most of the frequencies between 20 GHz and 60 GHz. If the array is large enough such that edge effects can be neglected, a -2 dB transmission coefficient suggests the overall antenna efficiency (e_{ant}) should be greater than 63%. The antenna efficiency is defined by IEEE as $e_{ant} = G\lambda^2/(4\pi A)$, where G is the antenna gain and A is the area. As the antenna is scanned to 45° and 60° from normal, the transmission degrades slightly and the axial ratio increases to 4 dB at some frequencies and scan directions. It is useful to compare the axial ratio of this antenna to that of an electric current sheet supporting x and y polarized currents with equal amplitude and 90° phase difference, which is often considered an ideal case. When the current sheet is scanned to 45° and 60°, the axial ratio is 3.0 dB and 6.0 dB, respectively (see Appendix). In other words, an ideal current sheet has a larger axial ratio at wide scan angles than the simulated antenna-polarizer combination reported here. Figure 43(d) shows the VSWR at broadside, 45°, and 60° scan angles along the E, H, and D planes. The VSWR remains below 3:1 at all scan angles between 20 GHz and 60 GHz. It should also be emphasized that no optimization was performed on this antenna-polarizer combination. It

is likely that the performance could be improved if the structures are optimized in the presence of each other.

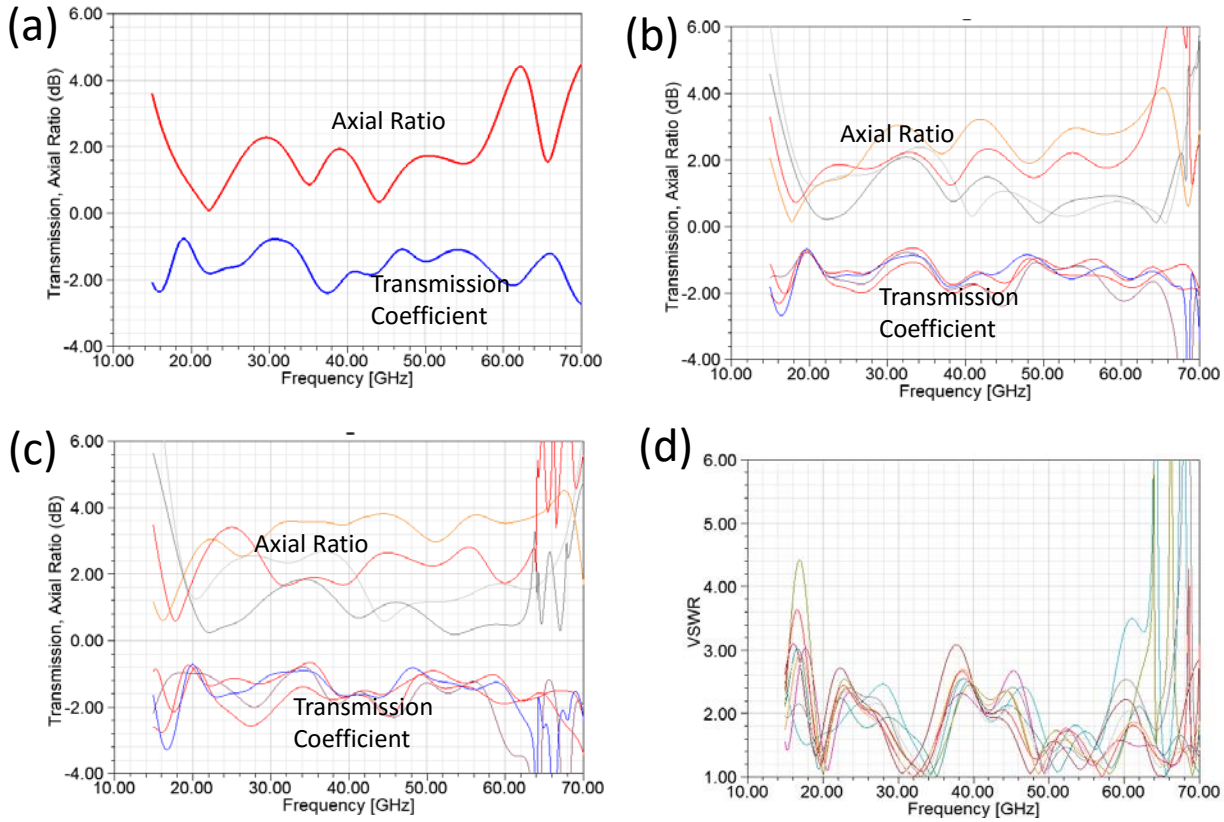

Figure 43: Performance of the Infinite Array Combined with the Linear-to-Circular polarizer when the radiates at broadside (a), 45° scan (b), and 60° scan (c)

6.4 Estimating Finite Polarizer Edge Effects

Thus far, both the Vivaldi array and linear-to-circular polarizer have been analyzed assuming they are infinitely large in area. Previous work has shown that finite arrays can perform comparable to infinite arrays if several rows of dummy cells are placed along the array periphery. These dummy cells should be terminated with matched resistors to reduce edge effects. It is also known that the linear-to-circular polarizer should be larger than the beam area if it is to behave similar to the infinite area case. As a general rule of thumb, quasi-optical components should have a diameter that is 1.5 times the diameter of an incident Gaussian beam to keep edge effects at a minimum [34]. However, having a polarizer with diameter that is 50% larger than the antenna is undesirable since this leads to a low aperture efficiency.

A simplified model for the finite antenna combined with a polarizer was studied in COMSOL (see Figure 44(a)). The simulation assumes the fields are invariant out of the plane, which reduces the simulation domain to two dimensions. This simplification allows for quick

simulations of electrically large geometries, which provides physical intuition. The polarizer is assumed to be a dielectric slab with 25 mm thickness and $\varepsilon = 3$. Impedance matching dielectrics are present at the front and back interfaces of the dielectric. An out-of-plane directed current sheet at the bottom of the simulation domain excites the geometry with a uniform amplitude excitation. The currents are phased to steer the beam to 60° from broadside since this represents the maximum desired scan angle, and edge effects are more significant as the scan angle increases.

The normalized far field radiated towards 60° vs. width of the dielectric slab (i.e. polarizer) is shown in Figure 44 and Figure 45. The figures correspond to the cases where the current sheet is 64 mm and 32 mm wide, to simulate a 32 element array and a 16 element array, respectively. In both cases, increasing the width of the polarizer reduces edge effects, which in turn increases the gain. Eventually, the gain levels off once the polarizer width is ~30 mm wider than that of the current sheet.

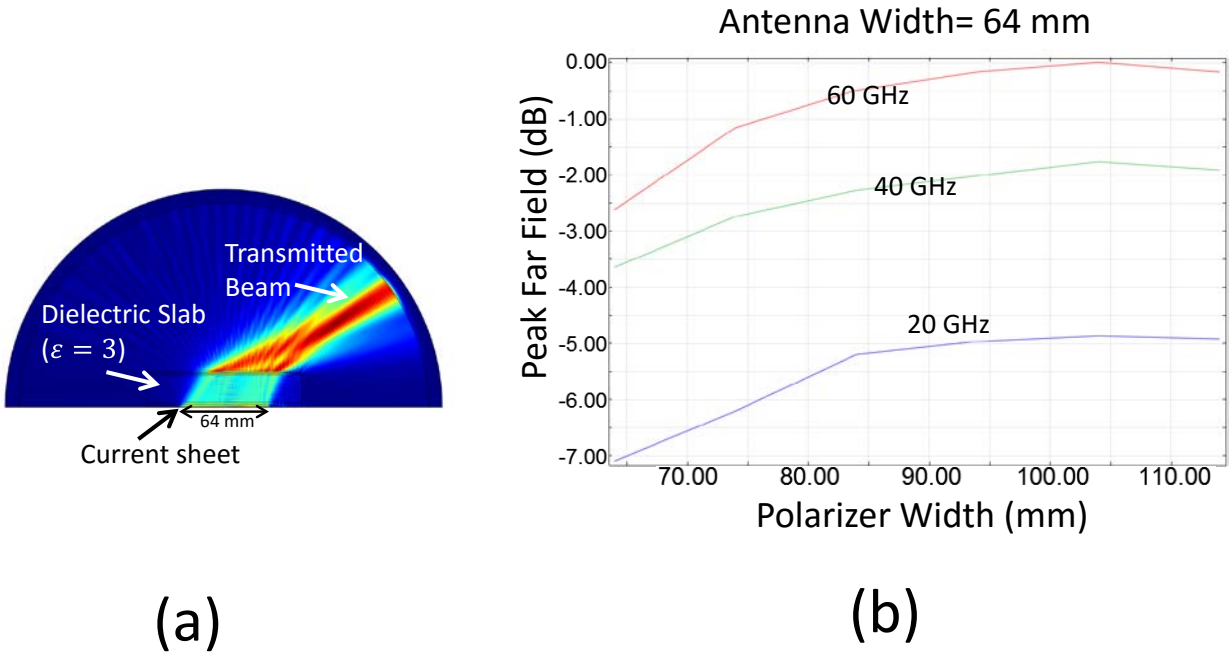

Figure 44: Electric Field Magnitude (a) and Normalized Far Field Radiated Towards $\theta = 60°$ (b) From a 64 mm Wide Array with Uniform Amplitude is Scanned

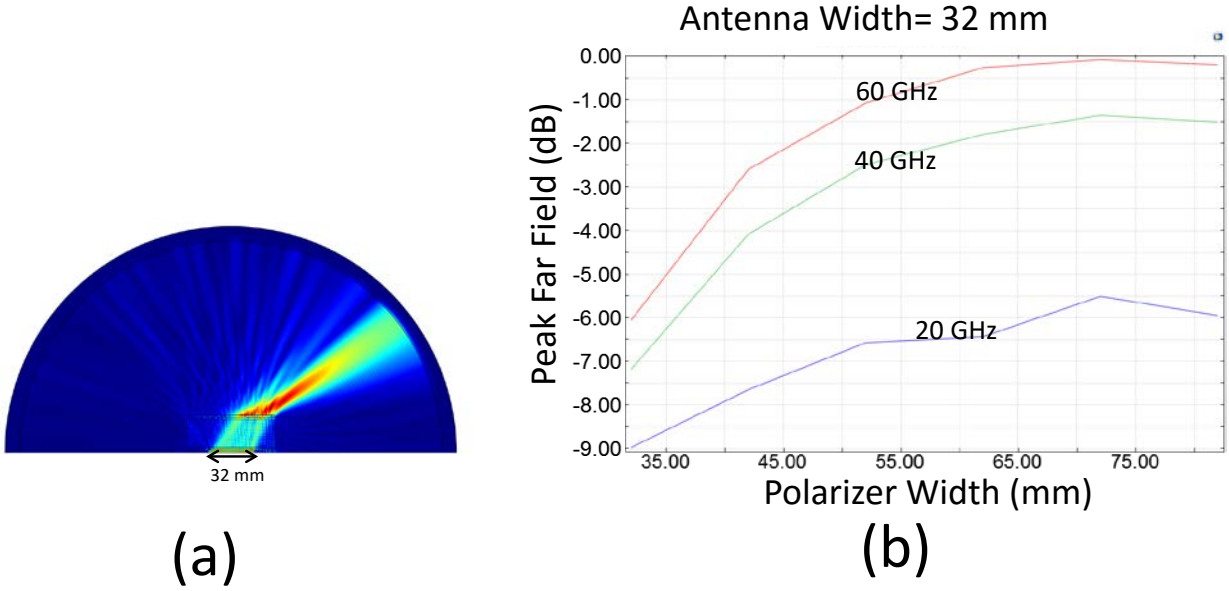

Figure 45: Electric Field Magnitude (a) and Normalized Far Field (b) When the Array is 32 mm Wide

These simplistic simulations inspired an intuitive method for estimating the required diameter of the polarizer (d_{pol}) vs. the antenna diameter (d_{ant}) and polarizer thickness (t_{pol}). If the current sheet is phased to radiate a beam that propagates toward θ in free space, the same wave propagates at $\text{asin}(\sin(\theta)/n_{pol})$ within the dielectric slab (i.e., polarizer) due to its increased refractive index. For the polarizers designed here, $n_{pol} \approx \sqrt{3}$ is the effective refractive index. Using a simple ray tracing approach shown in Figure 46, it is possible to estimate the required diameter of the polarizer (d_{pol}) such that edge effects are less significant,

$$d_{pol} > d_{ant} + \frac{2\, t_{pol} \sin(\theta)}{\sqrt{n_{pol}^2 - \sin(\theta)^2}} \tag{12}$$

This expression neglects diffraction, and therefore is more accurate as the array size (in terms of wavelengths) increases. If the array is less than 10λ in length, it is generally better to use polarizer diameter larger than that given in (12). This expression illustrates how increasing the polarizer thickness not only increases the thickness of the overall system, but also the required area. For the cascaded sheet impedance polarizer, $t_{pol} = 9$ mm and $n_{pol} \approx \sqrt{3}$, which suggests that the diameter of the polarizer should be at least 10 mm larger than that of the array if scanning up to 60° from broadside is required.

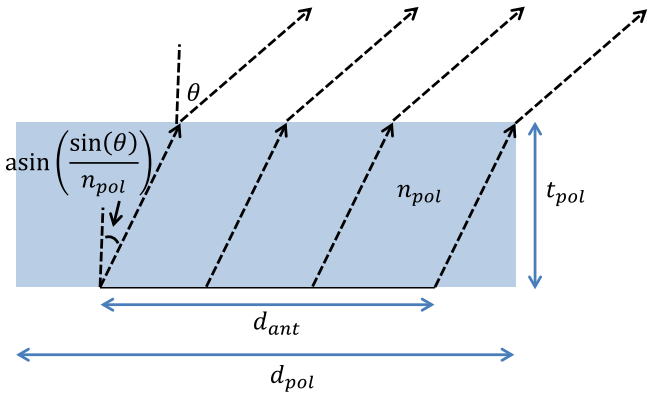

Figure 46: Ray Tracing Model Used to Estimate the Required Diameter of the Linear-to-Circular Polarizer Such that Edge Effects are Minimized

6.5 Corporate Beamformer

The microstrip feed lines behind the antenna must be connected to TR modules so that phase shifters, low noise amplifiers, power amplifiers, and switches can be integrated into every antenna element. The TR modules must then be combined in some manner so that signals at every antenna can be added coherently. There are many methods of combining the TR modules depending upon the number of desired channels for a particular application.

Here, the simplest approach is considered where every element is combined to a single port (i.e., single channel) using a corporate beamformer, as shown in Figure 47. It should be noted that losses in the beamformer are less important than losses in the antenna and polarizer since TR modules are placed between the beamformer and antennas. This beamformer is designed to feed a 256 element array (16 x 16 elements), but can be easily modified to feed any number of elements that is a power of 2. The beamformer consists of 8 cascaded Wilkinson power dividers. All power dividers are identical. Each Wilkinson power divider utilizes 3 stages to provide a wide bandwidth, and was optimized using HFSS. A single power divider and its performance are shown in Figure 48. The insertion loss of the power divider is 0.5 dB at 40 GHz, and the reflection coefficient at the input port is below -25 dB for most of the band. It is important to have a very good impedance match when many power dividers are cascaded together, or else resonances between the cascaded power dividers can notably degrade the performance. For example, simulations showed that when the reflection coefficient of a single power divider is increased such that it is below -15 dB throughout the band, the input reflection coefficient of 4 cascaded power dividers reaches -6 dB at some frequencies.

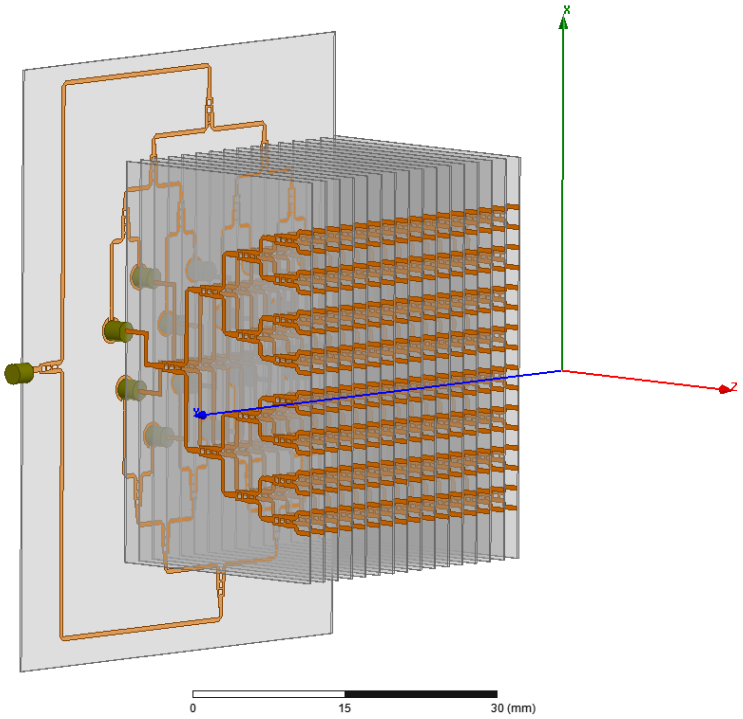

Figure 47: Designed 1:256 Corporate Beamformer

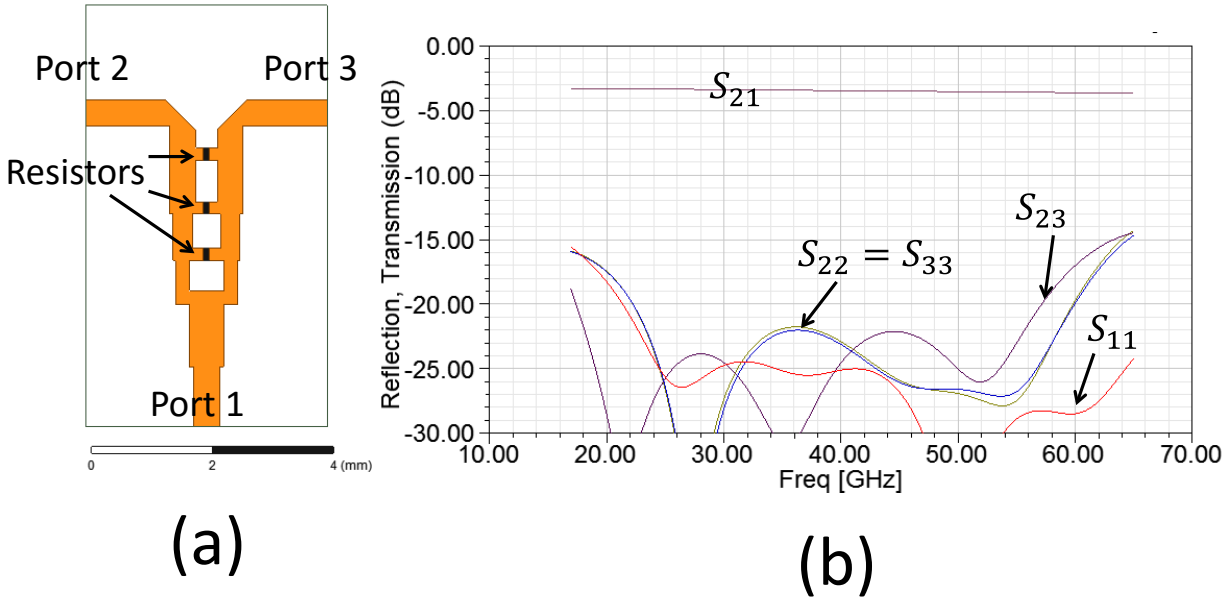

Figure 48: The 3-stage Wilkinson Power Divider Employed by the Corporate Beamformer (a), and its Performance (b)

The feed network utilizes 2 different sections. The first section (shown in Figure 49) is oriented in the *xy* plane of Figure 47. This section is a 1:16 power divider that feeds each column of the array. The second section (shown in Figure 50) consists of 16 different columns, each with 1:16 power dividers on them. The two different sections will be connected together using SMPM (i.e., GPP0) connectors. The 16 output ports of the first section are staggered to provide additional space for the SMPM connectors. The performance of the two different sections is shown in Figure 49(b) and Figure 50(b). The loss of the first section is notably larger than that of the second section, which primarily results from the increased length of microstrip lines required for feeding the staggered ports. It is expected that the total loss in the 1:256 beamforming network ranges from 5 dB to 15 dB as the frequency is increased from 20 GHz to 60 GHz. Note that the 10 dB higher insertion loss at the upper operating frequency is consistent with a transmission line resistance/unit length that is independent of frequency. Depending upon the performance of the TR modules, additional amplifiers may need to be integrated into the beamformer if this loss is too significant.

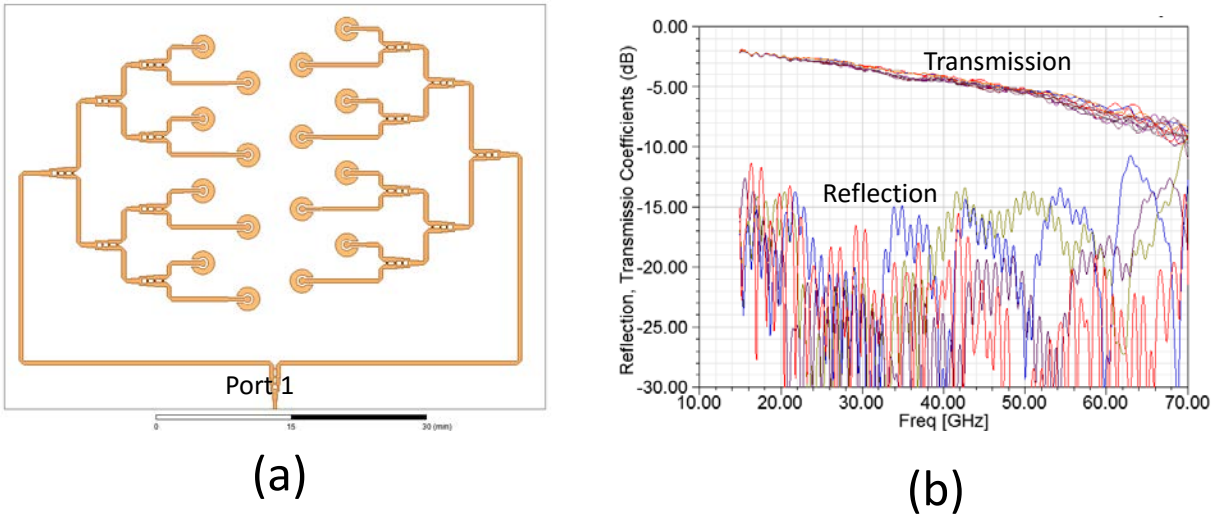

Figure 49: Geometry (a) and Performance (b) of the First Stage of the Corporate Beamformer Used to Feed Each Column of the Array

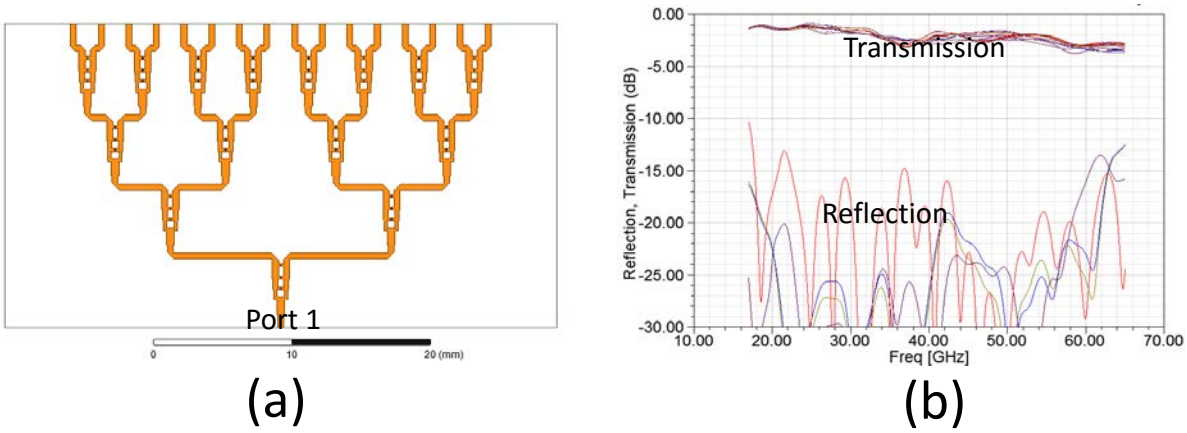

Figure 50: Geometry (a) and Performance (b) of the Second Stage of the Corporate Beamformer Used to Feed Each Vivaldi Element

6.6 Combining Everything Together

Although the entire 16 x 16 element array was not simulated, it is insightful to see how everything fits together, as shown in Figure 51 and Figure 52. The design employs 3 dummy cells at every edge of the array to reduce truncation effects. This adds an additional 12 mm in length to the array, such that the overall area of the array (including dummy cells) is 44 mm x 44 mm ($8.8\lambda_h \times 8.8\lambda_h$). The presence of these dummy cells doubles the area occupied by the array. In addition, it was previously noted that the linear-to-circular polarizer should be at least ~10 mm larger than the active part of the array to reduce its edge effects. Therefore, the linear-to-circular polarizer is also 44 mm x 44 mm in area. The first stage of the corporate feed network, which is oriented in the xy plane, is slightly larger than the array and polarizer, which unnecessarily reduces the aperture efficiency. In the future the microstrip lines on this feed network can be routed more compactly to reduce its area.

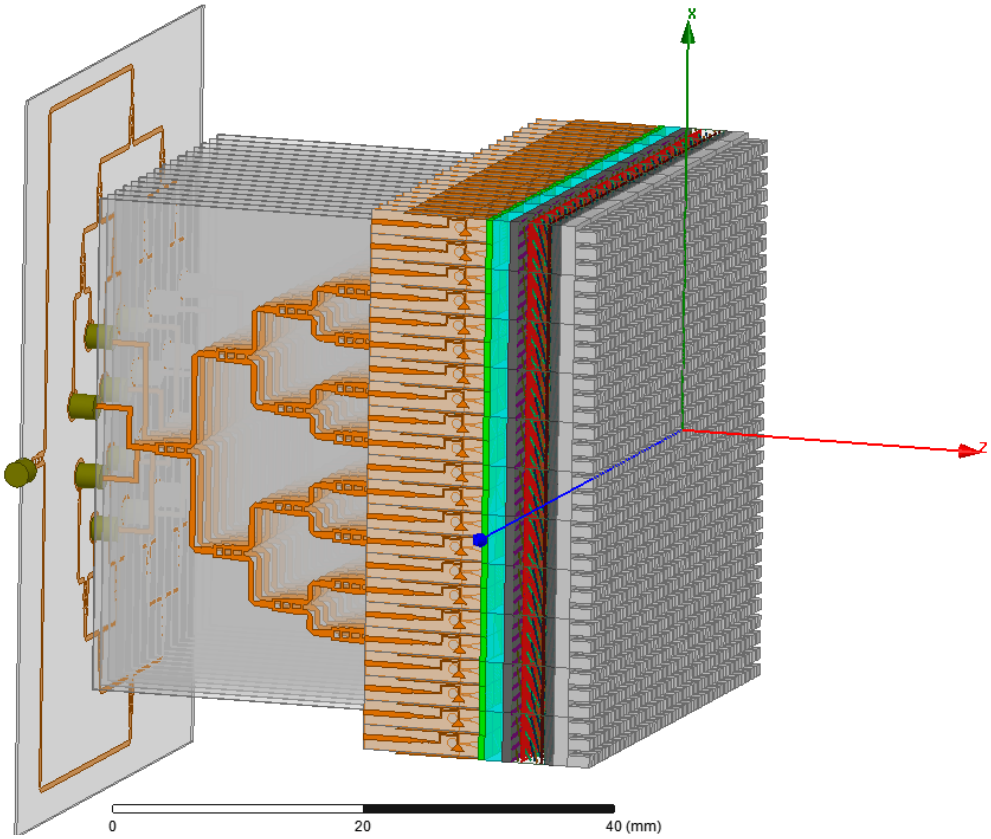

Figure 51: Designed Array Integrated with the Corporate Feed Network and the Linear-to-Circular Polarizer

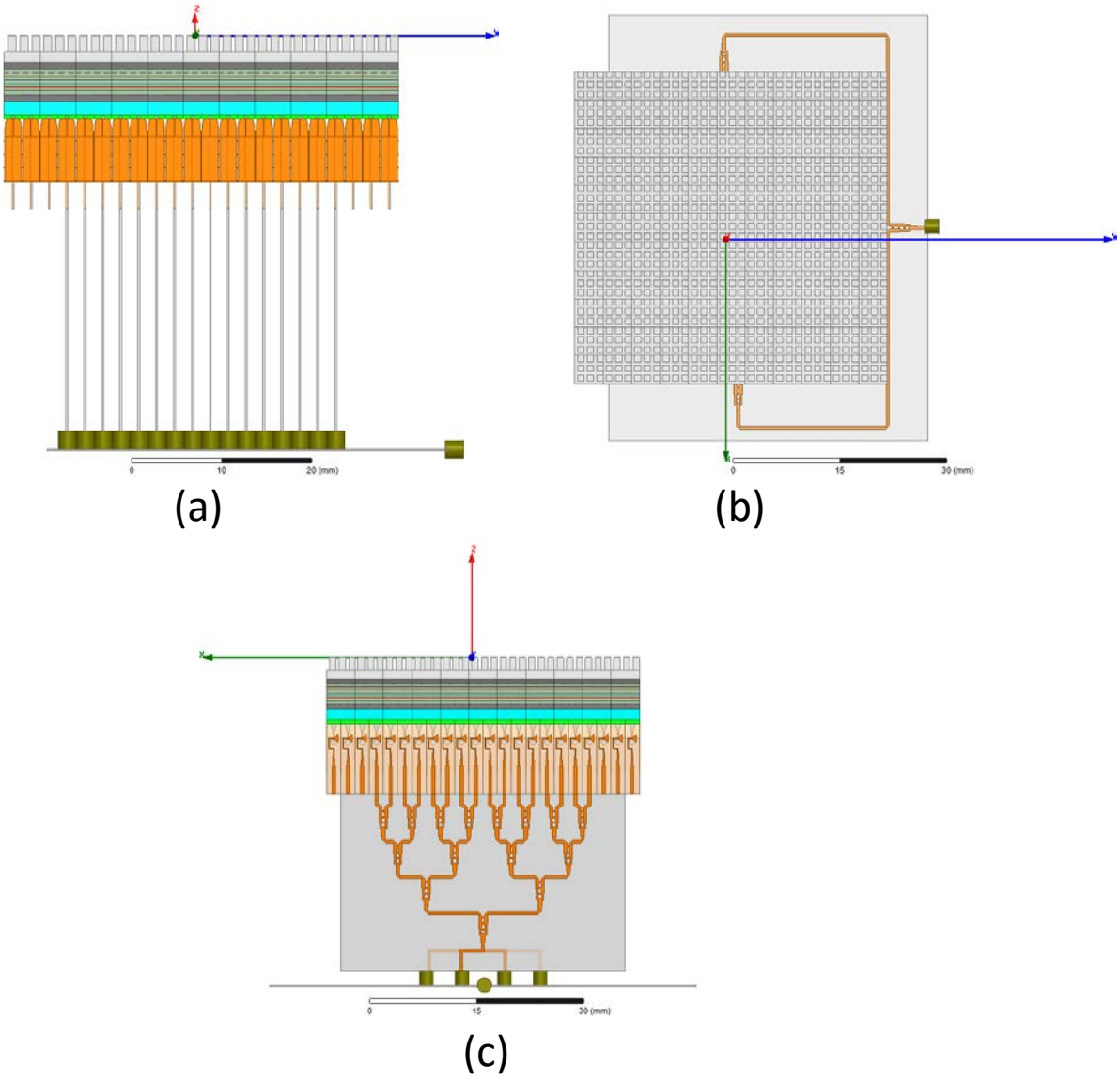

Figure 52: (a)-(c) Designed Array When Viewed from the Top, Front and Side, Respectively

6.7 Summary

Infinite array simulations suggest that the insertion loss from the microstrip feed of the radiating element to free space radiation (i.e., front-end loss) is ~2 dB, and the axial ratio is below 3 dB for most frequencies across the band. The array works for scan angles up to 60° from normal along arbitrary planes (E, H, and D planes were simulated). The insertion loss and axial ratio degrade by ~1 dB near the upper and lower frequencies and/or at wide scan angles near 60° along some planes. The edge effects of the linear-to-circular polarizer are estimated using a 2D simulation. The developed ray tracing model suggests that the linear-to-circular polarizer should be ~12 mm

larger in diameter than the active portion of the array to ensure it behaves similarly to the case where it is infinitely large. A 1:256 beamforming network with 5 to 15 dB of loss is designed as the frequency changes from 20 GHz to 60 GHz. The beamforming network, Vivaldi array, and linear-to-circular polarizer are drawn together to provide a concrete picture of the envisioned system.

7.0 Conclusions and Future Work

This report demonstrates that realizing the radiating aperture of a mm-wave, circularly polarized, wideband array with reasonable performance is feasible. The array operates at mm-wave frequencies (20-60 GHz), which imposes significant challenges from a design and fabrication perspective. To simplify the fabrication process, linearly polarized Vivaldi array elements in a column by column arrangement and respective feeds are implemented. Provisions were made for the integration of TR modules and a cooling system. A linear-to-circular polarizer is placed on the radiating aperture to radiate circular polarization. It is also shown for the first time that linear-to-circular polarizers with 4:1 bandwidths and wide angle scanning can be realized. The simulated transmission coefficient and axial ratio are roughly 60% and below 3 dB, respectively, across most of the band between 20 GHz and 60 GHz. In addition, the transmission and axial ratio only degrade by ~1 dB as the array is scanned from broadside to 60°.

In the future, the Vivaldi array should be co-optimized with the linear-to-circular polarizer to improve the performance of the cascaded system. Furthermore, the Vivaldi array should be fabricated, which is not trivial since it requires non-standard PCB assembly. Measurements of the array will illustrate the reliability of the fabrication process. Another area of the design that needs to be experimentally tested is the SMPS connectors used to attach the two beamforming stages together. In addition, significant work remains to be done to develop wideband TR modules and integrate them into the array. We also envision that research and development is required to properly cool the TR modules. Although some work remains to develop a fully functional system, this report provides a clear starting point that should inspire additional research and development in this area.

8.0 References

[1] R. W. Kindt and W. R. Pickles, "Ultrawideband all-metal flared-notch array radiator," *IEEE Transactions on Antennas and Propagation,* vol. 58, pp. 3568--3575, 2010.

[2] S. Livingston and J. J. Lee, "Evolution of wide band array designs," *IEEE International Symposium on Antennas and Propagation (APSURSI),* pp. 1957-1960, 2011.

[3] D. H. Schaubert, S. Kasturi, A. O. Boryssenko and W. M. Elsallal, "Vivaldi antenna arrays for wide bandwidth and electronic scanning," in *European Conference on Antennas and Propagation*, Edinburgh, UK, 2007.

[4] A. Jam and K. Sarabandi, "A horizontally polarized beam-steerable antenna for sub-millimeter-wave polarimetric imaging and collision avoidance radars," *IEEE International Symposium on Antennas and Propagation (APSURSI),* pp. 789-790, 2016.

[5] B. Doring, "Cooling system for a Ka band transmit antenna array," TU Berlin, 2006.

[6] T. Kamgaing, A. A. Elsherbini, S. N. Oster, B. M. Rawlings and K.-O. Lee, "Ultra-thin dual polarized millimeter-wave phased array system-in-package with embedded transceiver chip," *IEEE MTT-S International Microwave Symposium (IMS),* 2015.

[7] F. Golcuk, T. Kanar and G. M. Rebeiz, "A 90-100-GHz 4x4 SiGe BiCMOS Polarimetric Transmit/Receive Phased Array With Simultaneous Receive-Beams Capabilities," *IEEE Transactions on Microwave Theory and Techniques,* vol. 61, pp. 3099-3114, 2013.

[8] H. A. Wheeler, "Simple relations derived fom a phased-array antenna," *IEEE Trans. on Antenn. and Propag.*, vol. 13, p. 506, 1965.

[9] B. Munk, R. Taylor, T. Durharn, W. Croswell, B. Pigon, R. Boozer, S. Brown, M. Jones, J. Pryor, S. Ortiz and others, "A low-profile broadband phased array antenna," *IEEE Antennas and Propagation Society International Symposium,* vol. 2, pp. 448--451, 2003.

[10] A. Ludwig, "The definition of cross polarization," *IEEE Transactions on Antennas and Propagation,* vol. 21, pp. 116--119, 1973.

[11] B. A. Munk, "Chapter 18: Baluns, etc.," in *Antennas for All Applications, 3rd Edition,* Tata McGraw Hill, 2001.

[12] E. Magill and H. Wheeler, "Wide-angle impedance matching of a planar array antenna by a dielectric sheet," *IEEE Transactions on Antennas and Propagation,* vol. 14, pp. 49-53, 1966.

[13] S. S. Holland and M. N. Vouvakis, "The planar ultrawideband modular antenna (PUMA) array," *IEEE Transactions on Antennas and Propagation,* vol. 60, pp. 130-140, 2012.

[14] E. Yetisir, N. Ghalichechian and J. L. Volakis, "Ultrawideband Array With 70° Scanning Using FSS Superstrate," *IEEE Transactions on Antennas and Propagation,* vol. 64, pp. 4256-4265, 2016.

[15] R. J. Bolt, D. Cavallo, G. Gerini, D. Deurloo, R. Grooters, A. Neto and G. Toso, "Characterization of a dual-polarized connected-dipole array for Ku-band mobile terminals," *IEEE Transactions on Antennas and Propagation,* vol. 64, pp. 591--598, 2016.

[16] M. H. Novak and J. L. Volakis, "Ultrawideband antennas for multiband satellite communications at UHF-Ku frequencies," *IEEE Transactions on Antennas and Propagation,* vol. 63, pp. 1334-1341, 2015.

[17] J. D. Kraus, R. J. Marhefka and A. S. Khan, Antennas for All Applications, 3rd Edition, Tata McGraw-Hill Education, 2001.

[18] RF-Lambda, www.rflambda.com.

[19] Y. H. Choung, "Wideband double-slot cross-notch antenna," *IEEE Antennas and Propagation Society International Symposium*, pp. 448-451, 2001.

[20] S. Pancharatnam, "Achromatic combinations of birefringent plates," vol. 41, pp. 137-144, 1955.

[21] J.-B. Masson and G. Gallot, "Terahertz achromatic quarter-wave plate," *Optics Lett.*, vol. 31, pp. 265-267, 2006.

[22] G. Pisano, G. Savini, P. A. R. Ade, V. Haynes and W. K. Gear, "Achromatic half-wave plate for submillimeter instruments in cosmic microwave background astronomy: experimental characterization," *Applied Optics*, vol. 45, pp. 6982-6989, 2006.

[23] C. Pfeiffer and A. Grbic, "Millimeter-wave transmitarrays for wavefront and polarization control," *IEEE Trans. on Microwave Theory and Techniques*, vol. 61, pp. 4407-4417, 2013.

[24] S. M. A. M. H. Abadi and N. Behdad, "Wideband linear-to-circular polarization converters based on miniaturized-element frequency selective surfaces," *IEEE Trans. on Antenn. and Propag.*, vol. 64, pp. 525-534, 2016.

[25] L. Young, L. Robinson and C. Hacking, "Meander-line polarizer," *IEEE Trans. on Antenn. and Propag.*, vol. 21, pp. 376-378, 1973.

[26] D. Lerner, "A wave polarization converter for circular polarization," *IEEE Trans. on Antenn. and Propag.*, vol. 13, pp. 3-7, 1965.

[27] R.-S. Chu and K.-M. Lee, "Analytical method of a multilayered meander-line polarizer plate with normal and oblique plane-wave incidence," *IEEE Trans. on Antenn. and Propag.*, vol. 35, pp. 652-661, 1987.

[28] Thor Labs, https://www.thorlabs.com/.

[29] B. A. Munk, Finite antenna arrays and FSS, John Wiley & Sons, 2003.

[30] C. Pfeiffer and A. Grbic, "Emulating Nonreciprocity with Spatially Dispersive Metasurfaces Excited at Oblique Incidence," *Phys. Rev. Lett.*, vol. 117, p. 077401, 2016.

[31] K. F. Brakora, J. Halloran and K. Sarabandi, "Design of 3-D monolithic MMW antennas using ceramic stereolithography," *IEEE Trans. on Antenn. and Propag.*, vol. 55, no. 3, pp. 790-797, 2007.

[32] X. Chen, T. M. Grzegorczyk, B.-I. Wu, J. Pacheco Jr and J. A. Kong, "Robust method to retrieve the constitutive effective parameters of metamaterials," *Phys. Rev. E*, vol. 70, p. 016608, 2004.

[33] C. Pfeiffer and A. Grbic, "Bianisotropic metasurfaces for optimal polarization control: Analysis and synthesis," *Phys. Rev. Applied*, vol. 2, p. 044011, 2014.

[34] P. F. Goldsmith, "Quasi-optical techniques," *Proceedings of the IEEE*, vol. 80, pp. 1729-1747, 1992.

[35] A. Neto, D. Cavallo, G. Gerini and G. Toso, "Scanning performances of wideband connected arrays in the presence of a backing reflector," *IEEE Transactions on Antennas and Propagation*, vol. 57, pp. 3092--3102, 2009.

Appendix:
Axial Ratio Radiated By an Electric Current Sheet

Consider an electric current sheet ($\boldsymbol{J}_s$) directly on top of a perfect magnetic conductor such that radiation only occurs in the upper half space,

$$\boldsymbol{J}_s = \boldsymbol{x}J_x e^{-j(k_x x + k_y y)} + \boldsymbol{y}J_y e^{-j(k_x x + k_y y)}$$

where $\boldsymbol{x}$ and $\boldsymbol{y}$ are unit vectors. Enforcing $\boldsymbol{z} \times \boldsymbol{H} = \boldsymbol{J}$, and $\boldsymbol{k} \times \boldsymbol{H} = 0$ directly above the current sheet,

$$\boldsymbol{H} = -\boldsymbol{x}J_y + \boldsymbol{y}J_x + \boldsymbol{z}/k_z\left(k_x J_y - k_y J_x\right)$$

where $k_z = \sqrt{k_0^2 - k_x^2 - k_y^2}$ satisfies the separation relation in free space, and the common phase, $e^{-j(k_x x + k_y y + k_z z)}$ is neglected. The magnetic field can be decomposed into $\boldsymbol{\theta}$ and $\boldsymbol{\phi}$ components, $H_\theta = \boldsymbol{\theta} \cdot \boldsymbol{H}$ and $H_\phi = \boldsymbol{\phi} \cdot \boldsymbol{H}$,

$$H_\theta = \cos(\theta)\cos(\phi)\left(-J_y\right) + \cos(\theta)\sin(\phi)\left(J_x\right) - \sin(\theta)\left(1/k_z\left(k_x J_y - k_y J_x\right)\right)$$

$$H_\phi = \sin(\phi)\left(J_y\right) + \cos(\phi)\left(J_x\right)$$

where $\theta = \operatorname{acos}\left(\frac{k_z}{k_0}\right)$ and $\phi = \operatorname{atan}\left(\frac{k_y}{k_x}\right)$. The magnetic field is decomposed into right (H_{RH}) and left handed (H_{LH}) polarizations,

$$\begin{pmatrix} H_{RH} \\ H_{LH} \end{pmatrix} = \sqrt{2}\begin{pmatrix} 1 & 1 \\ -j & j \end{pmatrix}^{-1}\begin{pmatrix} H_\theta \\ H_\phi \end{pmatrix}$$

and the axial ratio is calculated,

$$AR = \frac{|H_{RH}/H_{LH}| + 1}{|H_{RH}/H_{LH}| - 1}$$

If we let $J_x = 1$ and $J_y = -j$, to radiate circular polarization, the axial ratio is 3 dB and 6 dB when the beam is scanned to 45° and 60° from normal respectively. Due to the symmetry of circular polarization, the axial ratio radiated by the current sheet is independent of the angle ϕ. It should be noted that if the x and y polarizations can be independently controlled, it is possible to radiate circular polarization with 0 dB axial ratio at an arbitrary angle by adjusting the ratio J_x/J_y. However, this would require twice as many TR modules, which adds cost.

List of Symbols, Abbreviations, and Acronyms

ACRONYM	DESCRIPTION
AESA	Active electronically scanned array
AR	Axial Ratio
D-plane	Diagonal plane ($\phi = \pm 45°$)
mm-wave	Millimeter-wave (30 GHz – 300 GHz)
PCB	Printed-circuit-board
S-parameters	Scattering parameters
TR Module	Transmit-receive module
VSWR	Voltage standing wave ratio
WAIM	Wide angle impedance matching layer
λ	Free space wavelegnth
λ_h	Free space wavelength at the highest operating frequency